

Probing cosmic-ray ion acceleration with radio-submm and gamma-ray emission from interaction-powered supernovae

Kohta Murase¹, Todd A. Thompson^{2,3}, and Eran O. Ofek⁴

¹*Hubble Fellow — Institute for Advanced Study, Princeton, New Jersey 08540, USA*

²*Center for Cosmology and AstroParticle Physics, The Ohio State University, Columbus, Ohio 43210, USA*

³*Department of Astronomy, The Ohio State University, Columbus, Ohio 43210, USA*

⁴*Benoziyo Center for Astrophysics, Weizmann Institute of Science, Rehovot 76100, Israel*

25 August 2021

ABSTRACT

The optical and near-IR emission from some classes of supernovae (SNe), including Type IIn and possibly some super-luminous SNe, is likely powered by a collision between the SN ejecta and dense circumstellar material (CSM). We argue that for a range of CSM masses and their radii, a collisionless shock can form, allowing for efficient cosmic-ray (CR) acceleration. We show that pp collisions between these newly accelerated CRs and the CSM leads to not only gamma rays but also secondary electrons and positrons that radiate synchrotron photons in the high-frequency radio bands. Our estimates imply that various facilities including the Jansky Very Large Array (VLA) and the Atacama Large Millimeter/submillimeter Array (ALMA) may observe such SNe at Gpc distances by followup observations in months-to-years, although the detectability strongly depends on the CSM density as well as observed frequency. Detecting this signal would give us a unique probe of CR acceleration at early times, and even non-detections can put interesting limits on the possibility of CR ion acceleration. Following our previous work, we also show that GeV gamma rays can escape from the system without severe attenuation, encouraging point-source and stacking analyses with *Fermi*. We provide recipes for diagnosing interaction-powered SN scenario with multi-messenger (neutrino and gamma-ray) observations.

Key words: non-thermal—supernovae

1 INTRODUCTION

Blind surveys for optical transients have revealed a class of super-luminous supernovae (SL) SNe that may in some cases be powered by a collision between the SN ejecta and a massive shell or wind of circumstellar material (CSM) (e.g., Falk & Arnett 1973; Ofek et al. 2007; Smith & McCray 2007; Quimby et al. 2011). Examples include SN 2003ma (Rest et al. 2011), 2006gy (e.g., Ofek et al. 2007; Smith et al. 2007; Smith et al. 2010), and 2008es (Miller et al. 2009), among others. As a consequence of the collision with the CSM, a significant fraction of the kinetic energy is converted into radiation via shock dissipation, which is responsible for the observed emission (see Figure 1).

The rate of SLSNe with absolute magnitude $M < -21$ is order of $\sim 10 \text{ Gpc}^{-3} \text{ yr}^{-1}$, $\sim 0.01\%$ of the normal

core-collapse SN rate (Gal-Yam 2012), but some normal-luminosity SNe such as SN 2005ip (Smith et al. 2009), 2006jc (Immler et al. 2008; Smith et al. 2008), 2008iy (Miller et al. 2010) and PTF 09uj (Ofek et al. 2010), which may also be powered by ejecta-CSM interactions, are more common (Quimby et al. 2013). Finally, recent observations of SN 2009ip and 2010mc suggest that the CSM eruption is timed to occur months-to-years before the core collapse (Mauerhan et al. 2013; Pastorello et al. 2013; Prieto et al. 2013; Ofek et al. 2013a; Margutti et al. 2014; Ofek et al. 2013c).

Interaction-powered SNe may be efficient cosmic-ray (CR) accelerators, where one can expect that the diffusive shock acceleration mechanism operates at the forward and reverse shocks by a collision between the SN ejecta and CSM. For a range of CSM parameters (mass and shock

dissipation radius), the shock is radiation-mediated — the Thomson optical depth is larger than c/V_s (Weaver 1976; Katz et al. 2010), where V_s is the shock velocity — and efficient CR acceleration is not expected because the CR collisionless mean free path is much shorter than the deceleration length. However, as the shock propagates in the CSM, photons can stream out ahead of the shock, and photon energy can no longer support the shock (i.e., shock breakout). After the breakout, for wind-like CSM profiles, the shock will become collisionless and CR acceleration can be efficient (Murase et al. 2011; Katz et al. 2011; Kashiyama et al. 2013). Recently, Murase et al. (2011) considered a collision between the SN ejecta with a CSM shell and found that CR protons may be accelerated, and furthermore that the protons may experience strong pionic losses via inelastic pp collisions, producing gamma-rays and neutrinos. Thus, interaction-powered SNe may be interesting CR accelerators and high-energy/multi-messenger emitters. In this work, we continue our study of the possibility of the non-thermal emission from the shock interaction of a SN embedded in a dense CSM. In particular, we focus on the secondary electrons and positrons expected from the same pp collisions that give rise to neutrinos and gamma rays. Importantly, we show that these secondaries can emit detectable synchrotron radiation at high-frequency radio wavelengths including mm/submm and FIR bands.

In Section 2, we review the shock physics and the potential for CR acceleration in interaction-powered SNe, providing a much more detailed discussion than Murase et al. (2011). Section 3 gives a brief discussion of the high-energy emission expected, and recipes that connect the observed optical emission to the non-thermal signatures are provided in Appendix A. In Section 4 we discuss high-frequency radio diagnostics. For a range of CSM parameters, we show that secondary leptons from pp interactions should radiate synchrotron at $\sim 3 - 3000$ GHz, and with fluxes of $\sim 0.01 - 0.1$ mJy at distances of hundreds of Mpc. In Section 5, we summarize our results.

Throughout this work, we use the notation $Q = Q_x 10^x$ in CGS unit unless we give notice.

2 BASIC SETUP

In this preparatory section, before we discuss non-thermal signatures, we explain the picture of interaction-powered SNe and describe the basic physical setup.

Let us consider SN ejecta with the kinetic energy \mathcal{E}_{ej} and the velocity V_{ej} . Noting $\mathcal{E}_{ej} = M_{ej}V_{ej}^2/2$ for the ejecta mass M_{ej} , the momentum and energy conservation laws give

$$M_{ej}V_{ej} + M_{cs}V_{cs} = (M_{ej} + M_{cs})V \quad (1)$$

$$\frac{1}{2}M_{ej}V_{ej}^2 + \frac{1}{2}M_{cs}V_{cs}^2 = \frac{1}{2}(M_{ej} + M_{cs})V^2 + \mathcal{E}_d, \quad (2)$$

where M_{cs} is the total CSM mass and $V_{cs} (< V_{ej})$ is the CSM

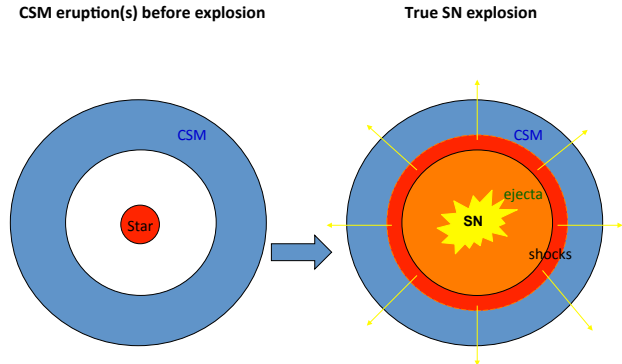


Figure 1. The schematic picture of the interaction-powered SN scenario.

velocity. The total dissipated energy \mathcal{E}_d is written as

$$\begin{aligned} \mathcal{E}_d &= \frac{M_{cs}}{M_{ej} + M_{cs}} \frac{1}{2} M_{ej} (V_{ej} - V_{cs})^2 \\ &\approx \frac{M_{cs}}{M_{ej} + M_{cs}} \mathcal{E}_{ej}, \end{aligned} \quad (3)$$

where $V_{ej} \gg V_{cs}$ is used in the last equality. The above equation suggests that a significant fraction of \mathcal{E}_{ej} can be dissipated if the CSM mass is large (see also, e.g., van Marle et al. 2010; Moriya et al. 2013b). Density profiles of both the ejecta and CSM are important for detailed predictions. For example, when the density profile of the ejecta is steep enough and most of its energy is carried by lower-velocity ejecta material, the explosion has driven waves that can be described by Chevalier-Nadezhin self-similar solutions (Chevalier 1982a). When the shock wave sweeps up ambient mass comparable to M_{ej} and it is non-radiative, we expect blast waves that can be described by Sedov-Taylor-like self-similar solutions (see Truelove & McKee 1999, and references therein). In this work, to push the basic idea and avoid uncertainty in the ejecta profile and many other complications due to radiation processes, we discuss non-thermal properties without relying on such details. Our treatment still provides an order of magnitude estimate of expected non-thermal signals, and a more detailed study will be presented in an accompanying paper (Murase et al. 2014).

Hereafter, we assume that the CSM has a wind-like power-law density profile and extends to the edge radius of the wind, R_w . We expect that this is reasonable (see, e.g., Ofek et al. 2014), although details are uncertain due to poor understandings of the CSM eruption mechanism. Then, the CSM density is written as

$$\rho_{cs} = DR_0^{-2} \left(\frac{R}{R_0} \right)^{-s} \simeq 5.0 \times 10^{16} D_* R_0^{-2} \left(\frac{R}{R_0} \right)^{-s} \text{ g cm}^{-3} \quad (4)$$

where R should be expressed in cm, $R_0 = 10^{15}$ cm, and D_*

is defined¹ for the mass-loss rate of $\dot{M}_{\text{cs}} \equiv 1 M_{\odot} \text{ yr}^{-1} \dot{M}_{\text{cs},0}$ and the wind velocity of $V_{\text{cs}} \equiv 10^3 \text{ km s}^{-1} (V_{\text{cs}}/10^3 \text{ km s}^{-1})$. This can also be expressed by

$$D \equiv \frac{\dot{M}_{\text{cs}}}{4\pi V_{\text{cs}}} \simeq 5.0 \times 10^{16} \dot{M}_{\text{cs},0} (V_{\text{cs}}/10^3 \text{ km s}^{-1})^{-1} \text{ g cm}^{-1}. \quad (5)$$

The CSM mass within R is estimated to be

$$M_{\text{cs}}(< R) = \int_{R_{\text{cs}}}^R dr 4\pi r^2 \rho_{\text{cs}}, \quad (6)$$

where R_{cs} is the CSM inner edge radius. In particular, in the wind case ($s = 2$), we have

$$M_{\text{cs}}(< R) = 4\pi D \Delta R \simeq 3.2 M_{\odot} D_* R_{16}, \quad (7)$$

where we have used $\Delta R \approx R$ and $R \equiv 10^{16} \text{ cm } R_{16}$. Note that, in the one-zone model where the calculation is performed for a CSM density n_{cs} at a given radius R , qualitative pictures for different density profiles are simply obtained by using M_{cs} instead of D_* (although the dynamics and temporal evolution depend on density profiles). The deceleration is significant after the ejecta accumulates the CSM mass equivalent to its own mass, whose radius is characterized by

$$R_{\text{dec}} \approx \frac{M_{\text{ej}}}{4\pi D} \simeq 10^{16} \text{ cm } (M_{\text{ej}}/10^{0.5} M_{\odot}) D_*^{-1}. \quad (8)$$

If $R_{\text{dec}} < R_w$, most of the ejecta energy is dissipated by the ejecta-CSM collision.

One of the important quantities is the Thomson optical depth. Using the CSM electron density,

$$n_e = \frac{DR^{-2}}{\mu_e m_H} \simeq 3.0 \times 10^8 \text{ cm}^{-3} \mu_e^{-1} D_* R_{16}^{-2}, \quad (9)$$

the Thomson optical depth is estimated to be

$$\tau_T^u = \int_R^{\infty} dr n_e \sigma_T \approx n_e \sigma_T R \simeq 2.0 \mu_e^{-1} D_* R_{16}^{-1}, \quad (10)$$

for $R < R_w$, where σ_T is the Thomson cross section. The Thomson optical depth in the downstream is also $\tau_T \approx n_e \sigma_T R$ although the density in the thin, interacting shell is compressed by the shock compression ratio. As seen below, the emission is mostly observed when $\tau_T \lesssim c/V_s$ after photons can leave the system. However, while the interaction with a dense CSM shell happens at $\tau_T \gtrsim$ a few, hard X rays and soft gamma rays produced at the shock cannot avoid Compton down-scattering and a significant fraction of the emission would be thermalized (Chevalier & Irwin 2012; Svirski et al. 2012; Pan et al. 2013). Equal lines of various optical depths, CSM density and luminosities in the (R, D) plane and (R, M_{cs}) plane are shown in Figures 2 and 3, respectively. The equal CSM density line, $D_* \simeq 33 R_{16}^2 n_{\text{cs},10}$, is also overlaid. Explanations for the optical depths other than the Thomson optical depth are given below. As argued by Murase et al. (2011), efficient CR acceleration is possible at $\tau_T \lesssim c/V_s$, and for $\tau_{\text{pp}} \gtrsim 1$ we expect almost all the accelerated CR ions to produce neutrinos, hadronic gamma rays, and secondary electrons and positrons. In the system,

¹ Another definition is $\rho_{\text{cs}} = D_* R^{-2}$ that is different from ours.

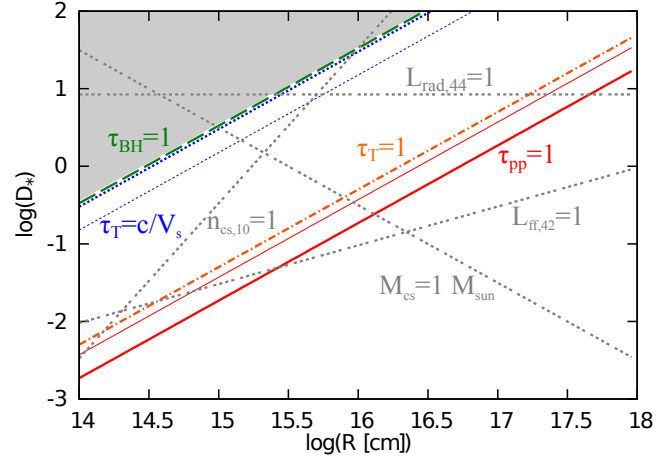


Figure 2. The parameter range allowing production and escape of gamma rays in the (R, D) plane. See the text for meanings of $\tau_T = c/V_s$, $\tau_T = 1$, $\tau_{\text{pp}} = 1$ and $\tau_{\text{BH}} = 1$. The shaded region suggests the range where we do not expect either production or escape of gamma rays. The thick curves represent $V_s = 5000 \text{ km s}^{-1}$ while the thin curves do $V_s = 10^4 \text{ km s}^{-1}$. With quadruplicate-dotted curves, lines of the constant CSM density ($n_{\text{cs}} = \text{const.}$), constant post-breakout radiation luminosity ($\epsilon_{\gamma} L_{\text{kin}} = \text{const.}$), constant optically-thin free-free luminosity ($L_{\text{ff}} = \text{const.}$), and constant CSM mass ($M_{\text{cs}} = \text{const.}$) are also shown for comparison.

hadronic gamma rays can interact with photons via the two-photon annihilation process and/or matter via the Bethe-Heitler (BH) pair-production process, respectively (see Section 3). The attenuation of GeV gamma rays due to the BH process is insignificant at $\tau_{\text{BH}} \lesssim 1$, which is not far from $\tau_T \lesssim c/V_s$.

In this work, we consider the forward shock, so the shock velocity V_s is regarded as the forward shock velocity V_f . The reverse shock power is smaller when the ejecta profile is steep (e.g., Chevalier & Fransson 2003). But this might not be the case if the profile is changed, e.g., possibly by experiencing many interactions with many CSM shells.

2.1 Early phase: subphotospheric interactions

When a collision with CSM occurs at $\tau_T \gg 1$, photons should experience many Compton scatterings, and it takes time for them to leave the system. The photon diffusion time is roughly $t_D \approx \Delta R^2 \sigma_T n_e / c$, which can further be approximated to be $t_D \approx \sigma_T \mu_e^{-1} D_* / c$ for the wind profile if $\Delta R \approx R$ (c.f. Chevalier & Irwin 2011; Balberg & Loeb 2012). Photons cannot essentially diffuse out from the system, when t_D is longer than the dynamical timescale is $t_{\text{dyn}} \approx R/V_s$. Hence, when the collision begins at $\tau_T \gtrsim c/V_s$, we start to observe a significant fraction of the emissions in the rise time t_{rise} such that $t_{\text{rise}} = t_D = t_{\text{dyn}}$ (e.g., Smith & McCray 2007; Ofek et al. 2010; Chevalier & Irwin 2011; Balberg & Loeb 2012). We define the breakout radius R_{bo} , where photons can essentially leave the system. When the effective diffusion radius R_D is sufficiently smaller than R_w (for $s \geq 2$), we have $R_{\text{bo}} \approx R_D$, and

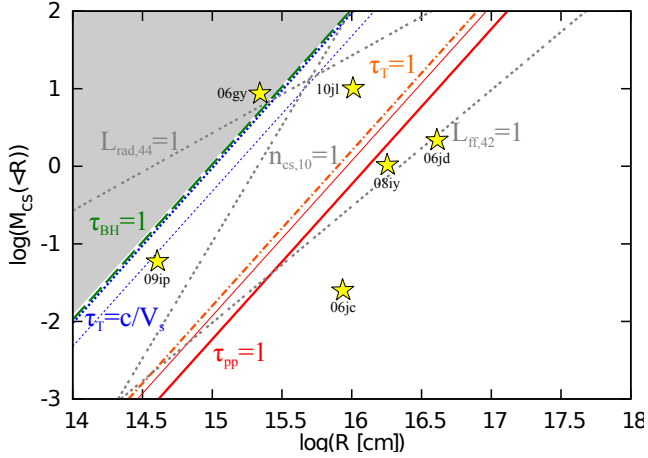


Figure 3. The same as Figure 2, but for the (R, M_{CS}) plane, where M_{CS} has the solar-mass unit. Lines of the constant CSM density ($n_{\text{CS}}=\text{const.}$), constant post-breakout radiation luminosity ($\epsilon_{\gamma}L_{\text{kin}}=\text{const.}$), and constant optically-thin free-free luminosity ($L_{\text{ff}}=\text{const.}$) are also shown for comparison. For explanations of specific SN examples, see Sub-section 2.6.

the shock breakout radius can be written as $R_{\text{bo}} \approx V_s t_{\text{rise}}$. When the CSM is so dense that R_D is larger than R_w , the rise time can be smaller than R_{bo}/V_s because $\Delta R \ll R_{\text{bo}} \approx R_w$ at the breakout (Chevalier & Irwin 2011).

We expect that thermal radiation carries a significant fraction ($\epsilon_{\gamma} < 1$) of the energy carried by the interacting shell (\mathcal{E}), where the radiated energy² is $\mathcal{E}_{\text{rad}} \equiv \epsilon_{\gamma} \mathcal{E}$ and \mathcal{E} after the collision is roughly comparable to \mathcal{E}_d (see Equation 3). Noting $\mathcal{E}/t_{\text{dyn}} \sim L_{\text{kin}} \approx (1/2)\rho_{\text{CS}}V_s^3(4\pi R^2)$, the (bolometric) radiation luminosity just after the breakout is

$$\begin{aligned} L_{\text{rad}} = \epsilon_{\gamma} L_{\text{kin}} &= \epsilon_{\gamma} \frac{1}{2} \rho_{\text{CS}} V_s^3 (4\pi R^2) \\ &\simeq 1.3 \times 10^{43} \text{ erg s}^{-1} (\epsilon_{\gamma}/0.3) \\ &\times D_* (V_s/5000 \text{ km s}^{-1})^3. \end{aligned} \quad (11)$$

The constant radiation luminosity line, $D_* \simeq 8.5(V_s/5000 \text{ km s}^{-1})^{-3} L_{\text{rad},44}$ (with $\epsilon_{\gamma} = 0.3$), is depicted in Figures 2 and 3. A more sophisticated model is given by Chevalier & Irwin (2011), which is summarized in Appendix A³.

2.2 Late phase: post-breakout interactions

The collision between the SN ejecta and the CSM may start from the optically-thick regime. Then, after the shock

breakout, the interaction eventually enters the optically-thin regime. This regime typically comes after the time of $\sim (c/V_s)(R_{\text{bo}}/V_s)$ when R_w is large enough. Hence, for optically SLSNe such as SN 2006gy, it usually happens only after the shock crosses $\sim R_w$. In order to expect optically-thin ejecta-CSM interactions within R_w , relatively large R_w and/or low M_{CS} are needed. Alternately, the collision may occur at $\tau_T \lesssim c/V_s$ if CSM effectively has an inner edge and can be regarded as a shell. Especially for optically-thin interactions at $\tau_T \lesssim 1$, hard X rays easily leave the system although ultraviolet photons and soft X rays may be attenuated due to bound-free absorption. Indeed, such X-ray and radio emissions have been observed in some SNe like SN 1988Z (Chugai & Danziger 1994; Ofek et al. 2013b) and 2006jd (Chandra et al. 2012a).

Let us consider a CSM extending to R_w . For $\tau_T(R_w) \lesssim c/V_s$, the characteristic duration of emission is expected to be $\approx R_w/V_s$ (or $\approx R_{\text{dec}}/V_s$). When the dominant loss process for thermal electrons is the free-free emission, the (bolometric) radiation luminosity mainly comes from bremsstrahlung emission. In the non-radiative case, we have (Rybicki & Lightman 1986; Chevalier & Fransson 2003)

$$\begin{aligned} L_{\text{rad}} \approx L_{\text{ff}} &= 4\pi \Lambda_{\text{ff}} n_e^2 R^2 \approx \Lambda_{\text{ff}} \frac{M_{\text{CS}} \sigma \rho_{\text{CS}}}{\mu_e^2 m_H^2} \\ &\simeq 1.1 \times 10^{42} \text{ erg s}^{-1} \bar{g}_{\text{ff}} \mu_e^{-2} \\ &\times D_{*,-1}^2 R_{16}^{-1} (V_s/5000 \text{ km s}^{-1}), \end{aligned} \quad (12)$$

where \bar{g}_{ff} is the Gaunt factor, Λ_{ff} for hydrogen is used, and absorption is not considered yet⁴. Here the compression factor σ is taken to be 4 but can be larger. The constant radiation luminosity line, $D_* \simeq 0.096 \bar{g}_{\text{ff}}^{-1/2} \mu_e R_{16}^{1/2} (V_s/5000 \text{ km s}^{-1})^{-1/2} L_{\text{ff},42}$, is depicted in Figures 2 and 3. When the shock is radiative, L_{rad} should be limited by the kinetic luminosity as in equation (11). It roughly occurs when the cooling time $t_{\text{ff}} \approx (3kT_e/\Lambda_{\text{ff}} n_{\text{CS}}) \simeq 3.1 \text{ yr } \bar{g}_{\text{ff}}^{-1} T_{e,8}^{1/2} D_{*,-1} R_{16}^2$ is shorter than time t . Note that L_{ff} is proportional to t^{-1} and $T_e \gtrsim 2 \times 10^7 \text{ K}$ is assumed, otherwise cooling by line emissions becomes relevant (e.g., Chevalier & Fransson 2003).

2.3 Shock properties

Whether efficient CR acceleration occurs or not depends on the shock properties. When an ejecta-CSM collision occurs at sufficiently small radii, the shock is initially radiation-mediated in the sense that the upstream shock structure is modified by radiation from the downstream. For non-relativistic shocks where effects of pairs are irrelevant, the shock is radiation-mediated when $\tau_T \gtrsim c/V_s$ (Weaver 1976; Katz et al. 2010). When coupling with radiation is strong enough, electrons transfer their energy to photons. In the

² For the adiabatic index $\hat{\gamma} = 4/3$, $\epsilon_{\gamma} = 0.32$ is obtained in the mini-shell model (Chevalier & Irwin 2011). See also Ofek et al. (2014).

³ For the purpose of modeling observed light curves, which is not the focus of this work, one may use expressions for more general profiles of $\rho_{\text{CS}} \propto R^{-s}$ and $\rho_{\text{ej}} \propto R^{-m}$ (Svirski et al. 2012; Ofek et al. 2014).

⁴ Even if the absorption is serious, X rays are detectable if the unattenuated X-ray luminosity is large enough, as suggested in SN 2010jl (Ofek et al. 2014).

thermal equilibrium limit, at the far downstream, photons, electrons and protons have the temperature of

$$kT_{\text{ph}} \simeq 1.2 \text{ eV } \tilde{\epsilon}_{\text{gb}}^{-1/4} D_*^{1/4} R_{16}^{-1/2} (V_s/5000 \text{ km s}^{-1})^{1/2}, \quad (13)$$

where $\tilde{\epsilon}_{\text{gb}} a T_{\text{ph}}^4 = (18/7) \rho_{\text{cs}} V_s^2$ is used and $\tilde{\epsilon}_{\text{gb}}$ is the gray-body factor. Note that this emission does not have to be the observed emission since photons start to escape only after $\tau_T \sim c/V_s$. Thermal equilibrium may not be realized if sufficient photons are not produced by the bremsstrahlung process (Chevalier & Irwin 2011; Svirski et al. 2012). At the nearer downstream, protons and electrons have much higher temperatures. In the absence of collisionless-plasma processes, the electron temperature is determined by the balance between Coulomb heating and cooling processes. When the relevant cooling process is the Compton cooling, we have (Waxman & Loeb 2001; Murase et al. 2011; Katz et al. 2011)

$$kT_e \sim 40 \text{ keV } \tilde{\epsilon}_\gamma^{-2/5}, \quad (14)$$

over the length scale of $V_s \nu_{ie}^{-1}$ (where ν_{ie} is the ion-electron collision frequency), where $\tilde{\epsilon}_\gamma = 2U_\gamma / (3\sigma n_{\text{cs}} kT_p)$, where U_γ is the energy density of photons. Note that the above equation is valid for sufficiently high-velocity shocks, since T_e is limited by the proton temperature T_p (Chevalier & Irwin 2012). In reality, collisionless-plasma processes can be faster than Coulomb collisional processes, where T_e can be higher than in equation (14), but should be lower than the equipartition temperature.

After $\tau_T \lesssim c/V_s$, the shock is no longer radiation-mediated, and we expect collisionless (or collisional) shocks. For strong, non-relativistic shocks, the proton temperature at the immediate downstream is

$$kT_p = \frac{2(\hat{\gamma} - 1)}{(\hat{\gamma} + 1)^2} m_p V_s^2, \quad (15)$$

where $\hat{\gamma}$ is the adiabatic index. When the adiabatic index is $\hat{\gamma} = 5/3$, we have a well-known result, $T_p = (3/16) m_p V_s^2$. The electron temperature is affected by energy transfer from protons, which may be Coulomb heating or faster collisionless plasma processes. If $\hat{\gamma} = 5/3$ and when electrons and protons achieve the equipartition, we have (e.g., Fransson et al. 1996; Chevalier & Fransson 2003; Ofek et al. 2014)

$$kT_e \simeq 24 \text{ keV } (V_s/5000 \text{ km s}^{-1})^2. \quad (16)$$

Therefore, in the interaction-powered SN scenario, we can naturally expect X rays via bremsstrahlung or inverse-Compton (IC) processes since electrons should be heated by the shock (e.g., Murase et al. 2011; Katz et al. 2011; Chevalier & Irwin 2012; Pan et al. 2013). Also, we may assume the material is highly ionized at least in the immediate upstream. Detections of X rays allow us to

⁵ Note that $\tilde{\epsilon}$ is defined for the downstream energy density. On the other hand, as in Murase et al. (2011), ϵ is defined for the total energy while ε is defined for the ram pressure of the upstream flow.

probe the existence of strong shocks, supporting the scenario (Katz et al. 2011; Ofek et al. 2013b). However, there are several complications. First, free-free emission may be suppressed if thermal electrons mainly cool via the IC process. Secondly, when the ejecta-CSM interaction occurs at $\tau_T \gtrsim 1$, hard X rays lose their energies in both the emission zone (downstream) and screen zone (upstream), and softer X rays are down-graded via bound-free absorption. If the amount of non-ionized atoms similarly exists in the far upstream, the bound-free optical depth for soft X rays is roughly estimated to be (e.g., Rybicki & Lightman 1986; Ofek et al. 2013b)

$$\tau_{\text{bf}}^u \simeq 600 D_* R_{16}^{-1} (h\nu/\text{keV})^{-2.5}, \quad (17)$$

at $h\nu \sim 0.03 - 10 \text{ keV}$. Naively, the X-ray luminosity is then (e.g., Fransson et al. 1996; Chevalier & Fransson 2003)

$$L_X \sim f_{\text{sup}} L_{\text{rad}} \frac{(1 - e^{-\tau})}{\tau} e^{-\tau^u}, \quad (18)$$

where f_{sup} is the suppression by other losses, $\tau \sim \tau_T$ is the optical depth in the emission zone and $\tau^u \sim \tau_T^u + \tau_{\text{bf}}^u$ is the optical depth in the screen zone. Predictions for both the thermal and non-thermal X rays depend on details including the frequency-dependent opacity and the ionization in the upstream (see Chevalier & Irwin 2012; Svirski et al. 2012; Pan et al. 2013, and references therein). This work does not study X-ray emissions in detail, since non-thermal X rays can be largely contaminated or masked by thermal X rays.

2.4 Particle acceleration

Now, we consider particle acceleration. CR acceleration may become efficient when the shock is no longer radiation-mediated and becomes collisionless, which can be realized when $\tau_T \lesssim c/V_s$ (Murase et al. 2011; Katz et al. 2011; Kashiyama et al. 2013). Strong small-scale magnetic fields are expected as a result from plasma instabilities, and MHD mechanisms such as the turbulent dynamo ⁶ can also play crucial roles especially in the downstream (e.g., Inoue et al. 2009; Inoue et al. 2012). In addition, CRs themselves excite turbulence via CR stream instabilities, which can be important in the upstream (see Bell 2004; Bell 2013; Bykov et al. 2013, and references therein). Since details of these processes are uncertain, for simplicity, we parameterize the magnetic field with the ratio of $B^2/8\pi$ to $\rho_{\text{cs}} V_s^2/2$ as $\varepsilon_B \equiv B^2/(4\pi \rho_{\text{cs}} V_s^2)$. Then, we obtain

$$B \simeq 4.0 \text{ G } \varepsilon_{B,-2}^{1/2} D_*^{1/2} R_{16}^{-1} (V_s/5000 \text{ km s}^{-1}). \quad (19)$$

⁶ For example, if SNe occur in superbubbles formed by multiple SNe, it is possible to expect turbulent magnetic fields driven by interactions with the inhomogeneous interstellar medium. Here, the CSM could also be highly turbulent and magnetized before the SN ejecta crashes, since the transiently erupted CSM would also form a shock via interactions with the interstellar medium. In addition, some observations have suggested that the CSM may be clumpy (e.g., Chugai & Danziger 1994; Smith et al. 2009), and the shocked CSM could achieve strong magnetic fields via the turbulent dynamo due to the ejecta-CSM interaction.

In the Bohm limit, the proton acceleration time scale is estimated to be (see a review Drury 1983)

$$\begin{aligned} t_{p-\text{acc}} &= \frac{20}{3} \frac{c^2}{V_s^2} \frac{E_p}{eBc} \\ &\simeq 0.67 \text{ s } \epsilon_{B,-2}^{-1/2} D_*^{1/2} R_{16} \\ &\times (V_s/5000 \text{ km s}^{-1})^{-3} (E_p/\text{GeV}), \end{aligned} \quad (20)$$

and the proton maximum energy is estimated by comparing it to various cooling time scales (see below). In the fully-ionized plasma (that is the case in the vicinity of the shock), the Coulomb cooling time of thermal protons (Shlickeiser 2002),

$$\begin{aligned} t_{p-C} &\approx \frac{(m_p c^2/\text{GeV})}{3.1 \times 10^{-16} n_e} \frac{8.3 \times 10^{-9} T_{e,4}^{3/2} + \beta_p^3}{2} \\ &\sim 2.4 \times 10^1 \text{ s } \mu_e^{-1} D_*^{-1} R_{16}^2 (V_s/5000 \text{ km s}^{-1})^3, \end{aligned} \quad (21)$$

where $\beta_p \sim V_s/c$ is assumed but the velocity of injected protons may be higher, depending on details of injection processes. The ratio between the two is $t_{p-\text{acc}}/t_{p-C} \sim 2.8 \times 10^{-2} \mu_e \epsilon_{B,-2}^{-1/2} D_*^{1/2} R_{16}^{-1} (V_s/5000 \text{ km s}^{-1})^{-6} (E_p/\text{GeV})$ when the upstream is cold enough. Hence, the Coulomb energy loss timescale is longer than their acceleration time, so CR proton acceleration is possible. Note that the Coulomb cooling is much less relevant in the immediate downstream, where the temperature is much higher.

As protons are accelerated above the pion production threshold, $\gamma_p > 1.37$, inelastic pp interactions occur, leading to production of electrons and positrons via $\pi^\pm \rightarrow \nu_\mu + \bar{\nu}_\mu + \nu_e(\bar{\nu}_e) + e^\pm$. Their minimum injection Lorentz factor is (Dermer 1986)

$$\gamma_h \approx \frac{1}{4} \frac{m_\pi}{m_e} \sim 68. \quad (22)$$

The important point here is that the minimum injection Lorentz factor is unique for hadronic injections, which is different from the case of primary electron acceleration.

Primary electrons can also be shock accelerated via the Fermi acceleration mechanism. However, the Larmor radius of thermal electrons is smaller than that of thermal protons. Thus, electrons need to be energized via some plasma processes to cross the shock length and to get injected to the Fermi acceleration process. In other words, the Larmor radius of relativistic electrons, $\gamma_e m_e c^2 / (eB)$, should be larger than that of thermal protons, $\sim cm_p V_s / (eB)$. The Lorentz factor of electrons that can be accelerated by the conventional shock acceleration mechanism satisfies

$$\gamma_e \gtrsim \frac{m_p}{m_e} \frac{V_s}{c} \simeq 31 (V_s/5000 \text{ km s}^{-1}). \quad (23)$$

Keeping this in mind and introducing the energy fraction (ϵ_e) and number fraction (f_e) of relativistic electrons distributed with a power law, the injection Lorentz factor of primary shock-accelerated electrons (γ_l) is expressed as

$$\begin{aligned} \gamma_l &\approx g_{q_e} \frac{\epsilon_e}{f_e} \frac{m_p}{m_e} \frac{V_s^2}{2c^2} \\ &\simeq 5.1 \epsilon_{e,-3} f_{e,-5}^{-1} (g_{q_e}/0.2) (V_s/5000 \text{ km s}^{-1})^2, \end{aligned} \quad (24)$$

where $g_{q_e} = 1/\ln(\gamma_e^M/\gamma_l)$ for $q_e = 2$ and $g_{q_e} = (q_e - 2)/(q_e - 1)$ for $q_e > 2$. Here, q_e is the injection spectral index of accelerated electrons and γ_e^M is the maximum Lorentz factor of accelerated electrons. Note that equation (24) is obtained from $\int d\gamma_e (dN_e/d\gamma_e) = f_e N_p$ and $\int d\gamma_e (\gamma_e m_e c^2) (dN_e/d\gamma_e) = \epsilon_e N_p m_p V_s^2 / 2$. The values of ϵ_e and f_e are uncertain. The CR spectra observed at the Earth imply $\epsilon_e \sim 10^{-3} - 10^{-2}$, and such values are inferred from modeling of radio emission from Type IIb SNe (e.g., Maeda 2012). Smaller values of $\epsilon_e \sim 10^{-4}$ are obtained in the leptonic scenario for young SN remnants (e.g., Katz & Waxman 2008). Sufficiently large values of f_e imply $\gamma_l \lesssim (m_p/m_e)(V_s/c)$, where other electron acceleration processes in the shock transition layer should be relevant, and the spectrum for $\gamma_l \lesssim \gamma_e \lesssim (m_p/m_e)(V_s/c)$ may be steeper than that for $\gamma_e \gtrsim (m_p/m_e)(V_s/c)$.

The energy carried by accelerated CRs can be summarized as follows. The CR acceleration is efficient only after the radiation escapes from the system and the strong shock jump is formed by collisionless shocks. Hence, if $\min[R_{\text{dec}}, R_w] < R_{\text{bo}}$, we do not expect many CRs. Normal SNe correspond to $R_{\text{bo}} < R_w < R_{\text{dec}}$, so only a fraction of the SN explosion energy \mathcal{E}_{ej} is converted to CRs at the time the shock reaches R_w . If the CSM is massive and $R_{\text{bo}} < R_{\text{dec}} < R_w$ (thus $\tau_T(R_{\text{dec}}) < c/V_s$), we expect $\mathcal{E}_d \approx \mathcal{E}_{\text{ej}}$, so a significant fraction of the SN explosion energy can be converted into the energy of CRs. The energy of accelerated CR protons in interaction-powered SNe ($\mathcal{E}_{\text{CRp}}^{\text{ipSN}}$) is roughly estimated to be

$$\mathcal{E}_{\text{CRp}}^{\text{ipSN}} = \begin{cases} \epsilon_p \mathcal{E}_d \approx \epsilon_p \mathcal{E}_{\text{ej}}, & (R_{\text{bo}} < R_{\text{dec}} < R_w) \\ \epsilon_p \mathcal{E}_d \approx \epsilon_p (M_{\text{cs}}/M_{\text{ej}}) \mathcal{E}_{\text{ej}} & (R_{\text{bo}} < R_w < R_{\text{dec}}) \\ \ll \mathcal{E}_{\text{ej}} & (\min[R_{\text{dec}}, R_w] < R_{\text{bo}}) \end{cases} \quad (25)$$

Here equation (3) is used. Note that, for $R_w < R_{\text{dec}}$ (i.e., $M_{\text{cs}} < M_{\text{ej}}$), only the fraction of the SN explosion energy can be dissipated by one collision. Also, ϵ_p is the energy fraction carried by CRs above $m_p c^2$, and $\epsilon_p \sim 0.1 - 0.3$ is typically used in the context of SN remnants.

2.5 Fate of cosmic rays: hadronuclear reactions

When particles are accelerated up to very high energies, high-energy gamma rays and neutrinos should be accompanied via hadronuclear interactions like the pp reaction. In particular, CR protons interact with nucleons while they are advected to the downstream, so neutrinos and pionic gamma rays are expected in the GeV-PeV range (Murase et al. 2011). By comparing the pp interaction time scale $(n_N \sigma_{pp} c)^{-1}$ and t_{dyn} , we get the pp optical depth as

$$\tau_{pp} \approx \sigma_{pp} n_{\text{cs}} R(c/V_s) \simeq 5.4 D_* R_{16}^{-1} (V_s/5000 \text{ km s}^{-1})^{-1}, \quad (26)$$

where $\sigma_{pp} \approx 3 \times 10^{-26} \text{ cm}^2$ is used. From Figures 2 and 3, one sees large parameter space satisfying $\tau_T \lesssim c/V_s$ and $\tau_{pp} \gtrsim 1$, where neutrinos and gamma rays provide promising signals of CR proton acceleration at collisionless shocks. Even if $\tau_{pp} \lesssim 0.1$, we can say that a significant fraction of

the CR energy is converted into hadronic emission via pp interactions. From equation (26), one sees $D_* \propto \tau_{pp} R V_s$ or $M_{cs}(< R) \propto \tau_{pp} R^2 V_s$. Thus, as seen from Figure 3, pp processes are typically efficient for ejecta-CSM interactions at radii of $R \lesssim 10^{16.5}$ cm, for $M_{cs} \sim 1M_\odot$. Note that pp interactions are relevant even in the optically-thin regime of $\tau_T \lesssim 1$.

2.6 Examples

We here discuss several examples of SNe to see if ejecta-CSM interactions satisfying $\tau_T \lesssim c/V_s$ and $\tau_{pp} \gtrsim 0.1$ are indeed indicated by recent observations.

First, we consider the optically-thick regime around the shock breakout. Observationally, the CSM nucleon density n_{cs} (or D_*) can be estimated from the radiation luminosity L_{rad} (or the radiated energy \mathcal{E}_{rad}) at the time of the shock breakout, the rise time t_{rise} , and the shock velocity V_s (or R_{bo} that is the radius at the shock breakout). Note that the approximation $\Delta R \approx R$ is valid when $R_w > R_D = \sigma_T \mu_e^{-1} D_* V_s / c$.

- SN 2006gy: SN 2006gy is one of the SLSNe (e.g., Smith et al. 2007; Ofek et al. 2007; Smith et al. 2010). The radiated energy is $\mathcal{E}_{rad}(t_{bo}) \approx 10^{51}$ erg and the breakout time is $t_{rise} \approx 60$ d (Smith & McCray 2007; Chevalier & Irwin 2011). The breakout radius is estimated to be $R_{bo} \approx 2 \times 10^{15}$ cm, corresponding to $V_s \sim 4000$ km s⁻¹. These observational parameters imply $D_* \sim 10$ (see Appendix A), leading to $n_{cs} \sim 10^{11}$ cm⁻³ and $M_{cs} \sim 8M_\odot$ within R_{bo} . These are roughly consistent with numerical modeling of optical light curves (Moriya et al. 2013a).

- SN 2009ip: SN 2009ip is one of the luminous Type IIIn SNe, which showed re-brightening in 2012. The radiated energy is $\mathcal{E}_{rad}(t_{bo}) \approx 1.3 \times 10^{49}$ erg and the rising time⁷ is $t_{rise} \approx 10$ d. The breakout radius is estimated to be $R_{bo} \approx 5 \times 10^{14}$ cm, corresponding to $V_s \sim 6000$ km s⁻¹. These observational parameters imply $D_* \sim 0.3$, $n_{cs} \sim 4 \times 10^{10}$ cm⁻³ and $M_{cs} \sim 0.05M_\odot$ within R_{bo} (Margutti et al. 2014), which are consistent with observational constraints (Ofek et al. 2013a).

In Figure 3, both of the examples roughly lie on the $\tau_T = c/V_s$ lines. The condition $\tau_{pp} > 1$ is satisfied, so neutrinos and gamma rays should be produced in the presence of CR protons. SN 2006gy almost lies on the constant luminosity line of $\epsilon_\gamma L_{kin} = 10^{44}$ erg s⁻¹. Note that $\mathcal{E}_d \approx \mathcal{E}_{ej}$ can be expected for SN 2006gy but not for SN 2009ip.

Next, we consider post-breakout emission in the later phase. For $\tau_T \lesssim c/V_s$, the shock crossing time $t_s \approx R_w/V_s$ or the deceleration time $t_{dec} \approx R_{dec}/V_s$ can also be used instead of t_{rise} . Then, one can observationally estimate n_{cs}

⁷ The actual shock breakout time scale will be shorter, by a factor of a few, than the visible-light rise time of the SN light curve, since the bolometric light curve of Type IIIn SNe seems to rise faster than the optical light curve. Therefore, with the exception of SN 2010jl, t_{rise} given here, are regarded as an upper limit.

(or D_*) from L_{rad} , t_s (or t_{dec}), and V_s . Alternatively, if we assume that the CSM is not completely ionized, then the X-ray measurements of the bound-free absorption can provide an estimate (or at least a lower limit) on $N_H \approx n_H R$. Two examples are given below.

- SN 2006jd: SN 2006jd was a Type IIIn SN, showing bright X-ray emission with the unabsorbed X-ray luminosity of $\sim 3 \times 10^{41}$ erg s⁻¹ in the 0.2 – 10 keV range (Chandra et al. 2012a). Radio emission was detected after ~ 400 d. With $V_s = 5000$ km s⁻¹, we expect $R = 4 \times 10^{16}$ cm at $t \sim 1000$ d. Then, with the temperature $kT_e \sim 60$ keV, $L_{ff} \sim 10^{42}$ erg s⁻¹ implies $n_{cs} \sim 4 \times 10^6$ cm⁻³ and $M_{cs} \sim 2M_\odot$ within R . This estimated CSM density is comparable to $n_{cs} \sim 3 \times 10^6$ cm⁻³ obtained with $s = 1.6$, $M_{cs,-3}/V_{cs,2} \approx 3.3$ (for $R_0 = 10^{15}$ cm), and $R = 4 \times 10^{16}$ cm (Chandra et al. 2012a). On the other hand, X-ray absorption allows us to estimate the column density of non-ionized hydrogen atoms (N_H) that may exist in the far upstream. It is also suggested that this density is different from values based on X-ray observations, which may imply that the CSM is highly ionized even in the far upstream so there are not many non-ionized atoms in the line of sight of X rays. However, detections of radio emission may imply the absence of too strong free-free absorption in the upstream.

- SN 2010jl: SN 2010jl was also a Type IIIn SNe, showing bright X-ray emission without radio detections. The unabsorbed X-ray luminosity of $\sim 7 \times 10^{41}$ erg s⁻¹ is obtained in the 0.2 – 10 keV range (Chandra et al. 2012b). However, Ofek et al. (2014) suggested a higher intrinsic luminosity and obtained $N_H \sim 10^{25}$ cm² from modeling of the optical emission in the early phase around t_{bo} , which is consistent with a value indicated by X-ray observations. With $V_s = 4000$ km s⁻¹, we expect $R = 10^{16}$ cm at $t \sim 300$ d, implying $n_{cs} \sim 10^9$ cm⁻³ and $M_{cs} \sim 10M_\odot$ at that time. Although there is uncertainty, the CSM with several solar masses is likely (Ofek et al. 2014; Fransson et al. 2013), and this energetic SN seems one of the promising targets of dedicated searches for neutrinos and gamma rays.

Based on these parameters, SN 2010jl has $\tau_{pp} > 1$, indicating efficient neutrino and gamma-ray production. On the other hand, $\tau_{pp} < 1$ is suggested for SN 2006jd, but the pp efficiency is still significant. SN 2006jd also lies on the constant luminosity line of $L_{ff} = 10^{42}$ erg s⁻¹. Note that another estimate is possible based on detailed modeling of radio SNe (e.g., Chevalier 1982b; Chevalier 1984; Chevalier 1998), although this work does not focus on such more model-dependent studies. Most of type IIIn SNe have not been seen by low-frequency radio observations, but we show that some of them may be detectable at high-frequency radio wavelengths including mm/submm and FIR bands (see below).

In the Figure 3, we indicate the above examples by stars for the purpose of demonstration. Note that their parameters have large uncertainty so such plots do not have to be very precise. Also, R increases as the observation time t , so one can ideally draw evolution curves in the (R, D) plane and (R, M_{cs}) plane. In addition to the four SNe, we indicate SN 2006jc and 2008iy, which are also likely to be interaction-

powered SNe. For SN 2006jc, we use $M_{cs} \sim 0.02M_{\odot}$ and $R = 9 \times 10^{15}$ cm at the X-ray peak time of $t \sim 110$ d based on Immler et al. (2008). For SN 2008iy, we adopt $M_{cs} \sim 1M_{\odot}$ and $R = 1.7 \times 10^{16}$ cm at the peak time of $t \sim 400$ d from Miller et al. (2010).

2.7 Maximum energy: possible Pevatrons

SN remnants have been largely believed to be the origin of Galactic CRs up to the knee of $10^{6.5}$ GeV (see a review Bell 2013, and references therein). It would also be interesting to consider interaction-powered SNe as potential accelerators of high-energy CRs. The maximum energy of accelerated protons, E_p^M , is determined by comparing t_{acc} to the cooling time t_{cool} and dynamical time t_{dyn} .

If the time scales of energy losses (including adiabatic losses) are long enough, the maximum energy is limited by the dynamical time,

$$t_{dyn} \approx \frac{R}{V_s} \simeq 2.0 \times 10^7 \text{ s } R_{16} (V_s/5000 \text{ km s}^{-1})^{-1}. \quad (27)$$

Then, the maximum energy is (Murase et al. 2011)

$$E_p^M \approx 3.0 \times 10^7 \text{ GeV } \varepsilon_{B,-2}^{1/2} D_*^{1/2} (V_s/5000 \text{ km s}^{-1})^2. \quad (28)$$

Note that the Larmor radius (r_L) of protons is smaller than the system size (R), where the protons are confined.

At small R and/or large D , the maximum energy is limited by energy losses. The pp cooling time of protons is expressed as

$$t_{pp} = \frac{1}{\kappa_{pp} \sigma_{pp} n_{cs} c} \simeq 7.4 \times 10^6 \text{ s } D_*^{-1} R_{16}^2, \quad (29)$$

where $\kappa_{pp} \approx 0.5$ is the proton inelasticity. Equating t_{p-acc} and t_{pp} gives (Murase et al. 2011)

$$E_p^M \approx 1.1 \times 10^7 \text{ GeV } \varepsilon_{B,-2}^{1/2} D_*^{-1/2} R_{16} (V_s/5000 \text{ km s}^{-1})^3. \quad (30)$$

Before CRs propagate in a galaxy, they need to escape from the system without significant losses (e.g., Caprioli et al. 2009; Ohira et al. 2010; Drury 2011). While the ejecta interacts with a CSM, CR escape may be limited by the free escape boundary l_{esc} , which could be determined, e.g., by magnetic field amplification processes or wave damping via ion-neutral collisions (Kulsrud & Cesarsky 1971). By comparing the diffusion length $(1/3)(cr_L/V_s)$ (in the Bohm limit) to l_{esc} , we obtain

$$E_p^{\max} \approx 3.0 \times 10^7 \text{ GeV } \varepsilon_{B,-2}^{1/2} D_*^{1/2} (l_{esc}/R) (V_s/5000 \text{ km s}^{-1})^2, \quad (31)$$

where E_p^{\max} is the maximum energy of escaping protons. If E_p^M is too low for CRs to escape within t_{dyn} , CRs are confined and their escape is non-trivial. If magnetic fields rapidly decay after the shock crossing time (as often supposed in gamma-ray bursts), the condition can be $t_{esc} \sim t_{dyn} < t_{cool}$, otherwise it depends on diffusion and adiabatic losses. As a reasonable condition for CRs not to be depleted, we here assume $l_{esc} \sim R$ and $\tau_{pp} < 1$.

In Figures 4 and 5, we show the parameter range allowing $E_p^{\max} = 10^{15.5}$ eV protons. Parameter space allowing for

higher E_p^{\max} is narrower. If an ejecta-CSM interaction occurs at $\tau_{pp} \gtrsim 1$, CRs are largely depleted. We need $M_{cs} \gtrsim M_{ej}$ to expect $\mathcal{E}_d \sim \mathcal{E}_{ej}$, and $R \gtrsim 10^{16}$ cm is typically favored for escaping CRs to avoid significant pp cooling.

Higher-energy protons can generate pairs via the BH process, which occurs at $E_p h\nu > m_p m_e c^4$, i.e., $E_p > 4.8 \times 10^5$ GeV $(h\nu/1 \text{ eV})^{-1}$. Sufficiently high-energy protons may dominantly lose their energies via the BH process, especially in the optically-thick regime. For $\tau_T \gtrsim 1$, the number density of thermalized photons is $n_{ph} \sim \tau_T L_{ph} / (4\pi R^2 c k T_{ph})$, where L_{ph} is the luminosity of thermalized (re-processed) photons and ϵ_{ph} is their energy fraction. Assuming $L_{ph} = \epsilon_{ph} L_{kin}$, the BH cooling time $t_{p-BH} \approx 1/(\kappa_{BH} \sigma_{BH} n_{ph} c)$ becomes

$$t_{p-BH} \simeq 3.4 \times 10^7 \text{ s } \epsilon_{ph}^{-1} \mu_e D_*^{-2} \times R_{16}^3 (V_s/5000 \text{ km s}^{-1})^{-3} (kT_{ph}/1 \text{ eV}), \quad (32)$$

where $\kappa_{BH} \sigma_{BH} \approx 7.6 \times 10^{-31} \text{ cm}^2$ is used at $h\bar{\nu} \sim 20m_e c^2$ in the proton rest frame (Chodorowski et al. 1992). This is typically longer than the pp cooling time, so we may mainly consider the pp reaction. As indicated in Figures 4 and 5, on the other hand, the optically-thin regime of $\tau_T < 1$ is more likely in cases where protons with $E_p \sim 10^{6.5}$ GeV survive. X-ray photons interact with TeV protons and the number density of optically-thin bremsstrahlung photons is $n_X \sim L_{ff} / (4\pi R^2 c k T_e)$, so we have

$$t_{p-BH} \sim 1.2 \times 10^{15} \text{ s } \mu_e^2 \bar{g}_{ff}^{-1} D_{*, -1}^{-2} \times R_{16}^3 (V_s/5000 \text{ km s}^{-1})^{-1} (kT_e/50 \text{ keV}), \quad (33)$$

which is negligible compared to t_{pp} . In addition, photomeson production may also occur at $E_p > 6.5 \times 10^7$ GeV $(h\nu/1 \text{ eV})^{-1}$. Although it seems that the proton energy has to be quite high, some interactions with X-ray photons are possible in the attenuation scale of X rays.

Finally, we briefly discuss a possible contribution of interaction-powered SNe to the observed Galactic CRs. Contributions from various types of SNe including ‘‘hypernovae’’⁸ have been considered (e.g., Sveshnikova 2003). It is still under debate which astrophysical accelerator is responsible for CRs around the knee, although normal SNe have been commonly believed as a leading candidate. An issue is how CR protons are accelerated up to the knee, and interaction-powered SNe could have some advantages because of higher densities and possible stronger fields. The observed CR energy flux at $E_2 = 10^{6.5}$ GeV is smaller than that at $E_1 = 1$ GeV by $\sim 2.8 \times 10^{-5}$. The contribution of interaction-powered SNe at E_2 compared to the contribution of normal SNe at E_1 is (e.g., Budnik et al. 2008)

$$\frac{E_2^2 \Phi_{CR}}{E_1^2 \Phi_{CR}} \approx \frac{\rho_{ipSN}}{\rho_{SN}} \frac{t_{conf}(E_2)}{t_{conf}(E_1)} \frac{\mathcal{E}_{CRp}^{ipSN}}{\mathcal{E}_{CRp}^{SN}} \frac{\mathcal{R}_p(E_1)}{\mathcal{R}_p(E_2)}, \quad (34)$$

where \mathcal{R}_p is the conversion factor from the total en-

⁸ Hypernovae are often defined as SNe with $\mathcal{E}_{ej} > 10^{52}$ erg, which are usually broadline Type Ibc SNe. Note that only a fraction of them are trans-relativistic SNe that show a mildly relativistic component.

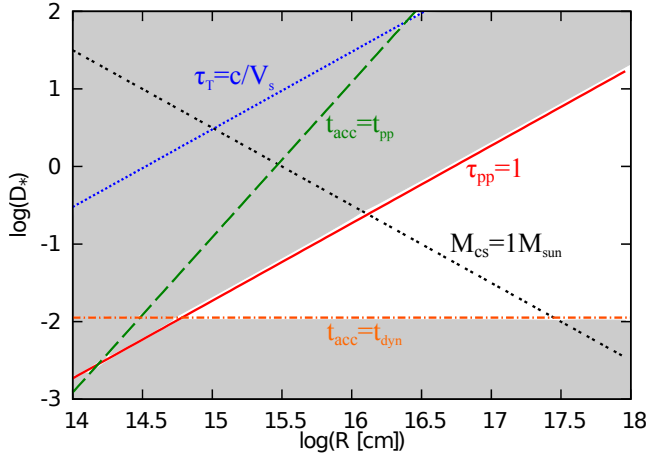


Figure 4. The parameter range allowing $E_p^{\max} = 10^{15.5}$ eV protons in the (R, D) plane. CR acceleration is possible at $\tau_T \lesssim c/V_s$ and $t_{\text{acc}} < t_{pp}$ and $t_{\text{acc}} < t_{\text{dyn}}$ are required to achieve $E_p^M = 10^{15.5}$ eV in the acceleration region. The shaded region suggests the range where we do not expect either production or escape of $10^{15.5}$ eV protons.

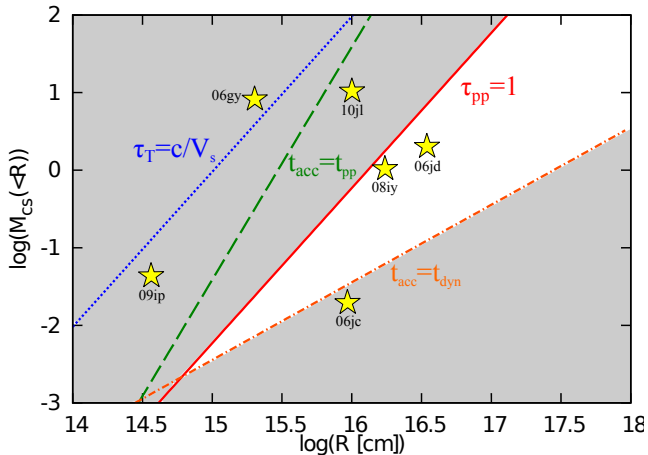


Figure 5. The same as Figure 4, but for the (R, M_{CS}) plane, where M_{CS} has the solar-mass unit.

ergy to the energy spectrum (see Appendix A), ρ_{ipSN} is the rate of interaction-powered SNe, ρ_{sn} is the SN rate, and t_{conf} is the confinement time of Galactic CRs. Although the confinement time is highly uncertain, if $t_{\text{conf}}(E_1)/t_{\text{conf}}(E_2) \sim (10^{6.5} \text{ GeV}/1 \text{ GeV})^{1/2} \sim 1800$ and $\mathcal{E}_{\text{CRp}}^{\text{ipSN}} \sim \mathcal{E}_{\text{CRp}}^{\text{sn}}$, interaction-powered SNe could contribute to the observed CR flux around the knee if the rate of interaction-powered SNe is as high as $\rho_{\text{ipSN}} \sim 0.05\rho_{\text{sn}}$.

3 HIGH-ENERGY NEUTRINO AND GAMMA-RAY DIAGNOSTICS

By taking into account the inelasticity $\kappa_{pp} \approx 0.5$, we obtain the effective pp optical depth as

$$f_{pp} \approx \kappa_{pp}\tau_{pp} \simeq 2.7 D_* R_{16}^{-1} (V_s/5000 \text{ km s}^{-1})^{-1}, \quad (35)$$

which gives the meson production efficiency. Using f_{pp} , the neutrino energy fluence (per flavor) is estimated to be

$$\begin{aligned} E_\nu^2 \phi^\nu &\approx \frac{1}{4\pi d^2} \frac{1}{6} \min[1, f_{pp}] E_p^2 \frac{dN_p}{dE_p} \\ &\simeq 1.4 \times 10^{-4} \text{ erg cm}^{-2} \min[1, f_{pp}] \left(\frac{E_\nu}{0.05 m_p c^2} \right)^{2-q_p} \\ &\times \epsilon_{p,-1} \mathcal{E}_{51} (d/10 \text{ Mpc})^{-2} \mathcal{R}_{p0,1}^{-1}, \end{aligned} \quad (36)$$

where q_p is the power-law index of the proton spectrum and \mathcal{R}_{p0} is $R_p \equiv \epsilon_p \mathcal{E} / (E_p^2 dN_p / dE_p)$ at $m_p c^2$ (see Appendix A). When the CSM mass is sufficiently large, assuming $f_{pp} < 1$ at the collision, we expect the typical energy fluence of $E_\nu^2 \phi^\nu \propto D_* R_{\text{dec}}^{-1} V_s^{-1}$ due to $\mathcal{E}_d \approx \mathcal{E}_{\text{ej}}$. On the other hand, when the CSM mass is not large enough, assuming $f_{pp} < 1$ at the collision, the typical energy fluence is expected to be $E_\nu^2 \phi^\nu \propto D_*^2 V_s^{-1}$ due to $\mathcal{E}_d \approx (M_{\text{CS}}/M_{\text{ej}}) \mathcal{E}_{\text{ej}}$. The typical neutrino energy is $E_\nu \sim 0.05 E_p$, so we expect GeV-PeV neutrino emission given that E_p^M reaches $\sim 10 - 30$ PeV. The IceCube effective area for muon neutrinos is order of 10^6 cm^2 in the 100 TeV range while $3 \times 10^3 \text{ cm}^2$ in the 1 TeV range, implying the fluence sensitivity of $\sim 10^{-4} \text{ erg cm}^{-2}$ (Ahrens et al. 2004). Hence, high-energy neutrinos are detectable by IceCube for nearby SNe that occur at $d \lesssim 10 - 20$ Mpc, and stacking analyses for aggregated signals from a number of interaction-powered SNe will also be useful (Murase et al. 2011). In Appendix A, we provide recipes that connect the observed optical emission to the neutrino signal.

The pionic gamma-ray energy fluence is 2 times larger than the neutrino fluence per flavor (after neutrino mixing), so we expect

$$\begin{aligned} E_\gamma^2 \phi^\gamma &\approx \frac{1}{4\pi d^2} \frac{1}{3} \min[1, f_{pp}] E_p^2 \frac{dN_p}{dE_p} \\ &\simeq 2.8 \times 10^{-4} \text{ erg cm}^{-2} \min[1, f_{pp}] \left(\frac{E_\gamma}{0.1 m_p c^2} \right)^{2-q_p} \\ &\times \epsilon_{p,-1} \mathcal{E}_{51} (d/10 \text{ Mpc})^{-2} \mathcal{R}_{p0,1}^{-1}, \end{aligned} \quad (37)$$

or using $E_p^2 dN_p / (dE_p dt) \sim \epsilon_p L_{\text{kin}} / \mathcal{R}_p$, the typical gamma-ray energy flux is

$$\begin{aligned} \nu F_\nu &\approx \frac{1}{4\pi d^2} \frac{1}{3} \min[1, f_{pp}] E_p^2 \frac{dN_p}{dE_p dt} \\ &\sim 1.1 \times 10^{-11} \text{ erg cm}^{-2} \text{ s}^{-1} \min[1, f_{pp}] \\ &\times \left(\frac{E_\gamma}{0.1 m_p c^2} \right)^{2-q_p} \epsilon_{p,-1} D_* \\ &\times (V_s/5000 \text{ km s}^{-1})^3 (d/10 \text{ Mpc})^{-2} \mathcal{R}_{p0,1}^{-1}. \end{aligned} \quad (38)$$

The *Fermi* 1 yr sensitivity at GeV energies is $\sim 3 \times 10^{-12} \text{ erg cm}^{-2} \text{ s}^{-1}$ (Funk & Hinton 2013), so interaction-powered SNe may be detectable with *Fermi* for power-

ful explosions at $d \lesssim 20 - 30$ Mpc (Murase et al. 2011). Stacking analyses are useful for GeV gamma rays as well as neutrinos (see Appendix A). In addition, future ground Cherenkov detectors will be more sensitive. For example, the CTA 100 hr sensitivity at TeV is $\sim 10^{-13}$ erg cm $^{-2}$ s $^{-1}$ (CTA Consortium 2011), whereas the HAWC 3 yr sensitivity at 2 TeV is $\sim 3 \times 10^{-12}$ erg cm $^{-2}$ s $^{-1}$ (Abeysekara et al. 2013). If the CR spectrum is as hard as $q_p \sim 2$, we expect that detections are possible up to $d \lesssim 100 - 200$ Mpc via followup observations by CTA within days-to-years.

For extragalactic gamma rays, one has to keep in mind attenuation processes. There are two effects: attenuation by the extragalactic background light (EBL) and attenuation by target photons in the source. The attenuation by EBL is relevant above $\sim 10 - 100$ TeV (Murase et al. 2011; Kashiyama et al. 2013), so we can neglect it to discuss the detestability in the GeV-TeV range. The attenuation in the source can be relevant especially for emission from the reverse shock, but we show below that gamma rays from the shocked CSM can typically escape from the source after the shock breakout, $\tau_T \lesssim c/V_s$.

3.1 Bethe-Heitler pair-creation process

Gamma rays around MeV energies are downgraded via Compton scattering with electrons in the matter. The BH pair-creation process occurs at $E_\gamma \geq 2m_e c^2$ and becomes dominant over the Compton scattering above the GeV range, where the Compton scattering is reduced by the Klein-Nishina suppression. At sufficiently high energies, the approximate cross section of the BH process is (Chodorowski et al. 1992)

$$\sigma_{\text{BH}} \approx \frac{3\alpha}{8\pi} \sigma_T \left[\frac{28}{9} \ln \left(\frac{2E_\gamma}{m_e c^2} \right) - \frac{218}{27} \right]. \quad (39)$$

Then, the BH opacity for gamma rays is expressed as

$$\tau_{\text{BH}} \approx \sigma_{\text{BH}} n_e R = \frac{\sigma_{\text{BH}}}{\sigma_T} \tau_T \simeq 0.03 D_* \mu_e^{-1} R_{16}^{-1}, \quad (40)$$

where σ_{BH} is evaluated at $E_\gamma = 1$ GeV. The parameter space such that $\tau_{\text{BH}} < 1$ is shown in Figures 2 and 3. Interestingly, it is comparable to the parameter space such that $\tau_T < c/V_s$ for typical shock velocities, since gamma-ray attenuation due to the BH process is irrelevant when V_s is higher than $c\sigma_{\text{BH}}/\sigma_T \sim 4500$ km s $^{-1}$.

Note that the BH opacity may be even smaller. Several observations have suggested that CSM is clumpy rather than uniform. The BH opacity becomes irrelevant when the CSM is anisotropic or so clumpy that most of the CSM mass is concentrated in dense clumps. For example, if the density enhancement in the clumps is $\delta\rho/\rho \sim 100$, the BH opacity is changed by $f_{\text{clu}} = (\delta\rho/\rho)^{-2/3} \sim 0.05$, where the attenuation by the BH process becomes even less relevant.

3.2 Two-photon annihilation process

Gamma rays interact with photons via $\gamma + \gamma \rightarrow e^+ + e^-$. The interaction typically happens at $E_\gamma h\nu \approx m_e^2 c^4$, and the

$\gamma\gamma$ opacity for sufficiently high-energy gamma rays is

$$\tau_{\gamma\gamma} \approx \frac{3}{16} \sigma_T (\nu n_\nu) R, \quad (41)$$

where νn_ν is the photon number density at ν .

When the collision with CSM occurs at $\tau_T \gtrsim$ a few, most of the emissions are thermalized. Using $\nu n_\nu \sim n_{\text{ph}} \sim L_{\text{ph}} \tau_T / (4\pi R^2 c k T_{\text{ph}})$, we obtain

$$\tau_{\gamma\gamma} \simeq 1.6 \times 10^3 \epsilon_{\text{ph}} \mu_e^{-1} D_*^2 R_{16}^{-2} (V_s/5000 \text{ km s}^{-1})^3 (k T_{\text{ph}}/1 \text{ eV})^{-1} \quad (42)$$

at $E_\gamma \approx 260$ GeV ($k T_{\text{ph}}/1$ eV) $^{-1}$. Above this energy, interactions mainly happen in the Klein-Nishina regime, so the $\gamma\gamma$ opacity decreases as $\propto \ln[0.47 E_\gamma k T_\gamma / (m_e^2 c^4)] E_\gamma^{-1}$.

Hard X rays, which can be produced by bremsstrahlung emission in the downstream, could potentially prohibit lower-energy gamma rays from leaving the emission region because the pair-creation threshold energy is lower for target photons with higher energies. Using $E_\gamma h\nu \approx m_e^2 c^4$ and $h\nu \sim k T_e$, the typical energy of gamma rays interacting with X-ray photons is estimated to be

$$E_\gamma \sim 5.2 \text{ MeV} (k T_e/50 \text{ keV})^{-1}. \quad (43)$$

As explained below we expect that GeV gamma rays can leave the system without significant attenuation. First, we consider an optically-thin collision at $\tau_T \lesssim 1$ with $L_{\text{rad}} \approx L_{\text{ff}}$. The black-body approximation is invalid, and hard X-ray emission becomes largely visible. The number density of optically-thin bremsstrahlung photons is $n_X \sim L_{\text{ff}} / (4\pi R^2 c k T_e)$, so we obtain

$$\begin{aligned} \tau_{\gamma\gamma} &\sim 4.5 \times 10^{-4} \mu_e^{-2} \bar{g}_{\text{ff}} \\ &\times D_{*, -1}^2 R_{16}^{-2} (V_s/5000 \text{ km s}^{-1}) (k T_e/50 \text{ keV})^{-1}, \end{aligned} \quad (44)$$

so gamma rays will be able to leave the emission region for ejecta-CSM interactions at $\tau_T \lesssim 1$.

The radiation luminosity may be limited by the kinetic luminosity, and interactions with X rays can be relevant in the length scale of $\sim (n_e \sigma_T)^{-1}$ even in the optically-thick regime of $1 \lesssim \tau_T \lesssim c/V_s$. Then, we may roughly expect

$$\tau_{\gamma\gamma} \sim 0.016 \epsilon_\gamma D_* R_{16}^{-1} (V_s/5000 \text{ km s}^{-1})^3 (k T_e/50 \text{ keV})^{-1}, \quad (45)$$

and $\tau_{\gamma\gamma} \sim 0.49 \epsilon_\gamma \mu_e (V_s/5000 \text{ km s}^{-1})^2 (k T_e/50 \text{ keV})^{-1}$ at R_{bo} . Therefore, given $\epsilon_\gamma < 1$, GeV gamma rays would be able to escape from the system. Note that the BH attenuation is also avoidable for sufficiently high shock velocities.

4 HIGH-FREQUENCY RADIO DIAGNOSTICS

Electrons and positrons (for which we simply say electrons) can generate synchrotron emission. The synchrotron cooling time of relativistic electrons is

$$\begin{aligned} t_{e-\text{syn}} &\approx \frac{6\pi m_e c}{\sigma_T B^2 \gamma_e} \\ &\simeq 4.9 \times 10^6 \text{ s } \gamma_{e,2}^{-1} \epsilon_{B,-2}^{-1} \\ &\times D_{*, -1}^{-1} (V_s/5000 \text{ km s}^{-1})^{-2} R_{16}^2. \end{aligned} \quad (46)$$

On the other hand, the IC cooling timescale is

$$t_{e-IC} = \frac{6m_e c}{\sigma_T B^2 \gamma_e Y_{IC}}, \quad (47)$$

where $Y_{IC} = Y_{SSC} + Y_{EIC}$ is the Compton Y parameter, Y_{SSC} is the synchrotron self-Compton (SSC) Y parameter, and Y_{EIC} is the external inverse-Compton (EIC) Y parameter. The IC emission is bolometrically more important than the synchrotron emission if $Y_{IC} > 1$. We expect that the SSC emission is typically weak. This is because the SSC Y parameter in the Thomson regime (e.g., Sari & Esin 2001),

$$Y_{SSC} \sim \frac{-1 + \sqrt{1 + 4\eta(\epsilon_l/\epsilon_B)(V_s/c)}}{2} \sim \eta(\epsilon_l/\epsilon_B)(V_s/c), \quad (48)$$

is less than unity. Here, $\eta = \min[1, (\gamma_c/\gamma_i)^{2-q}]$ and $\epsilon_l = \epsilon_e$ (or ϵ_\pm), where $\gamma_i = \gamma_l$ (or γ_h) is the injection Lorentz factor and γ_c is the cooling Lorentz factor defined below. External radiation fields are mainly supplied by SN emission, which is more relevant in our cases. If the system is optically thin, the energy density of thermal photons is

$$U_{rad} \approx \frac{L_{rad}}{4\pi R^2 c} \simeq 0.027 \text{ erg cm}^{-3} L_{rad,42} R_{16}^{-2}, \quad (49)$$

whereas the magnetic field energy density is

$$U_B = \frac{B^2}{8\pi} \simeq 0.064 \text{ erg cm}^{-3} \epsilon_{B,-2} \\ \times D_{*, -1} R_{16}^{-2} (V_s/5000 \text{ km s}^{-1})^2. \quad (50)$$

Because of $U_B > U_{rad}$, we see that the synchrotron cooling would be typically stronger than the EIC cooling, although the situation can be altered depending on parameters such as ϵ_B . As a result, non-thermal X rays can be expected mainly due to EIC emission. But they will be weaker than thermal X rays (except at hard X rays), and this work focuses on radio signals.

In the dense CSM environment, one also has to care about other losses such as bremsstrahlung and Coulomb losses. The relativistic bremsstrahlung cooling time scale is (Shlickeiser 2002)

$$t_{e-\text{ff}} \approx \frac{\pi}{3\alpha\sigma_T c n_{cs} (\ln \gamma_e + \ln 2 - 1/3)} \\ \simeq 5.2 \times 10^7 \text{ s } D_{*, -1}^{-1} R_{16}^2 (\ln \gamma_{e,2})^{-1}, \quad (51)$$

which is longer than t_{dyn} , $t_{e-\text{syn}}$ and t_{e-IC} for our typical parameters. The Coulomb loss time scale of relativistic electrons is (Shlickeiser 2002)

$$t_{e-C} \approx \frac{\gamma_e}{0.75c\sigma_T n_e (60 + \ln[\gamma_{e,2}/n_{e,8}])} \\ \simeq 2.2 \times 10^8 \text{ s } \gamma_{e,2} \mu_e D_{*, -1}^{-1} R_{16}^2, \quad (52)$$

which suggests that sufficiently high-energy electrons typically cool via the synchrotron emission. At lower energies, however, the Coulomb loss can be the shortest time scale, and the resulting synchrotron spectrum becomes complicated.

The cooling Lorentz factor is given by equating $t_{\text{dyn}}^{-1} =$

$t_{e-\text{syn}}^{-1} + t_{e-IC}^{-1}$ as

$$\gamma_c \approx 25 \epsilon_{B,-2}^{-1} D_{*, -1}^{-1} R_{16} (V_s/5000 \text{ km s}^{-1})^{-1} (1 + Y_{IC})^{-1}. \quad (53)$$

If $\gamma_c < \gamma_i$, the system is in the fast cooling regime, so the energy flux has a peak at $\nu_i \approx \gamma_i^2 eB/(m_e c)$. If $\gamma_i < \gamma_c$, the system is in the slow cooling regime, so the energy flux has a peak at $\nu_c \approx \gamma_c^2 eB/(m_e c)$.

Primary protons with $\gamma_p > 1.37$ lead to inelastic pp reactions, providing secondary electrons. The characteristic frequency of electrons with γ_h is

$$\nu_h \sim 1.0 \times 10^{11} \text{ Hz } \epsilon_{B,-2}^{1/2} D_{*, -1}^{1/2} R_{16}^{-1} (V_s/5000 \text{ km s}^{-1}). \quad (54)$$

For our typical parameters, $D_* \sim 0.01 - 1$ and $R \sim 10^{15} - 10^{17}$ cm, we expect $\nu_h \sim 3 - 3000$ GHz. We here point that these secondary electrons can be more relevant in the interaction-powered SN scenario. Very naively, the secondary electronic emission dominates over the primary electronic emission when

$$\epsilon_\pm \approx \frac{1}{6} \min[1, f_{pp}] \epsilon_p > \epsilon_e, \quad (55)$$

which is likely to be realized if f_{pp} is as high as $\sim 0.1 - 1$. One should keep in mind that this is the crude argument applied to the bolometric emission, and the relative importance changes with frequency, depending on spectral energy distributions of CR protons and electrons. Assuming the fast cooling regime, the resulting synchrotron flux from hadronically-injected electrons (at $\nu > \nu_h$) is

$$\nu F_\nu^h \approx \frac{1}{4\pi d^2} \frac{1}{12} \min[1, f_{pp}] E_p^2 \frac{dN_p}{dE_p dt} \\ \sim 2.7 \times 10^{-14} \text{ erg cm}^{-2} \text{ s}^{-1} \\ \times \min[10, f_{pp,-1}] \left(\frac{\nu}{\nu_h}\right)^{2-q_p} \epsilon_{p,-1} \\ \times D_{*, -1} (V_s/5000 \text{ km s}^{-1})^3 \mathcal{R}_{p0,1}^{-1} (d/10 \text{ Mpc})^{-2} \quad (56)$$

which corresponds to $F_\nu^h \sim 0.03 \text{ Jy } (d/10 \text{ Mpc})^{-2} \nu_{11}^{-1}$ for $q_p \sim 2$. Hence, the synchrotron signal is detectable with high-frequency radio telescopes when several absorption processes we discuss below are irrelevant. In particular, the ALMA sensitivity at 100 GHz is $\sim 6 \times 10^{-18} \text{ erg cm}^{-2} \text{ s}^{-1}$, allowing detections up to $d \sim 0.3 - 1$ Gpc if followup observations are successful.

Primary electrons can also emit synchrotron photons, and the corresponding characteristic frequency of electrons with γ_l is

$$\nu_l \approx 5.8 \times 10^8 \text{ Hz } \epsilon_{e,-3}^2 f_{e,-5}^{-2} (g_{qe}/0.2)^2 \epsilon_{B,-2}^{1/2} \\ \times D_{*, -1}^{1/2} R_{16}^{-1} (V_s/5000 \text{ km s}^{-1})^5. \quad (57)$$

It suggests that studying radio SNe at relatively low frequencies can probe electron acceleration in the shock transition layer, whereas investigations at high frequencies allow us to see the conventional shock acceleration of electrons and/or hadronic injections. The synchrotron energy flux (at $\nu > \nu_l$)

in the fast cooling case is

$$\begin{aligned} \nu F_\nu^l &\approx \frac{1}{4\pi d^2} \frac{1}{2} E_e^2 \frac{dN_e}{dE_e dt} \\ &\sim 1.6 \times 10^{-15} \text{ erg cm}^{-2} \text{ s}^{-1} \left(\frac{\nu}{\nu_l} \right)^{2-q_e} \epsilon_{e,-3} \\ &\times D_{*, -1} (V_s/5000 \text{ km s}^{-1})^3 \mathcal{R}_{e0,1}^{-1} (d/10 \text{ Mpc})^{-2}, \end{aligned} \quad (58)$$

where q_e is the electron spectral index and we expect $F_\nu^l \sim 0.002 \text{ Jy} (d/10 \text{ Mpc})^{-2} \nu_{11}^{-1}$ for $q_e \sim 2$. Note that q_e may naturally be different from values expected in the conventional diffuse shock acceleration theory at $\lesssim 2.1 \times 10^{10} \text{ Hz} \epsilon_{B,-2}^{1/2} D_{*, -1}^{1/2} R_{16}^{-1} (V_s/5000 \text{ km s}^{-1})^3$, corresponding to electrons with $\gamma_e \lesssim (m_p/m_e)(V_s/c)$, and steep indices of $q_e \sim 3$ are indeed indicated in non-relativistic radio SNe. The synchrotron signal from primary electrons is also detectable by current radio telescopes and mm/submm facilities including ALMA if secondary electrons are subdominant. For a given ν , the secondary electronic emission dominates over the primary electronic emission when

$$\min[10, f_{pp,-1}] \frac{\epsilon_{p,-1}}{\epsilon_{e,-3}} \left(\frac{\nu_l}{\nu_h} \right)^{2-q} \gtrsim 0.06, \quad (59)$$

where the fast cooling regime is assumed for $q_p = q_e = q$. Hence, we expect that secondaries are typically more important for high-frequency radio emission from interaction-powered SNe.

However, detecting radio signals may suffer from scattering and various absorption processes. First, if $\tau_T \gtrsim$ a few, the synchrotron emission can be modified by Comptonization due to thermal electrons. In particular, thermal electrons in the hot downstream may up-scatter low-energy photons. The condition that the Comptonization does not change the synchrotron spectrum is roughly given by $y_{\text{NR}} \approx (4kT_e/m_e c^2) \max[\tau_T, \tau_T^2] \lesssim 1$, so we focus on ejecta-CSM collisions satisfying $D_{*, -1} \lesssim 19 T_{e,8}^{-1/2} \mu_e R_{16}$. In addition, there are three important absorption processes that can hinder observations at the radio band, Razin-Tsyrovich (RT) suppression, synchrotron self-absorption (SSA) and free-free absorption. We discuss these suppression and absorption processes below.

4.1 Razin-Tsyrovich suppression

Synchrotron emission in a plasma is different from that in a vacuum. When a cold plasma plays a role⁹, it is suppressed at low frequencies due to collective effects. The suppression occurs at the RT frequency (Rybicki & Lightman 1986),

$$\begin{aligned} \nu_{\text{RT}} &\equiv \frac{2ecn_e}{B} \\ &\simeq 8.6 \times 10^9 \text{ Hz} \epsilon_{B,-2}^{-1/2} \mu_e^{-1} D_{*, -1}^{1/2} \\ &\times (V_s/5000 \text{ km s}^{-1})^{-1} R_{16}^{-1}. \end{aligned} \quad (60)$$

⁹ This may not be true in a relativistic plasma.

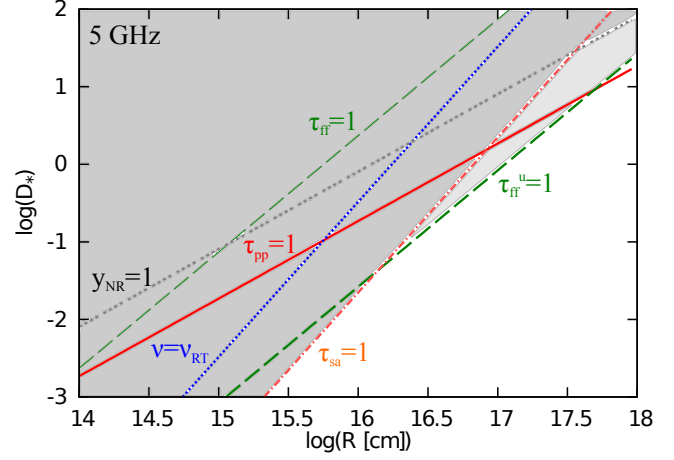


Figure 6. The parameter range allowing radio emission in the (R, D) plane, at $\nu = 5 \text{ GHz}$, where $V_s = 5000 \text{ km s}^{-1}$, $\epsilon_B = 10^{-2}$ and $\tilde{f} = 10^{-2.5}$ and $\gamma_i = \gamma_h$ are used. The suppression or absorption of radio emission is insignificant at $\tau_{\text{sa}} < 1$, $\nu > \nu_{\text{RT}}$, $\tau_{\text{ff}} < 1$ and $\tau_{\text{ff}}^u < 1$. The light shaded region indicates the forbidden region for the radio emission in the pessimistic case, where the upstream is assumed to be ionized with $T_e^u = 10^5 \text{ K}$. The dark shaded area indicates the forbidden region in the optimistic case, which may be realized for different upstream properties. The downstream temperature is set to $kT_e = 50 \text{ keV}$. From this figure, one sees that radio emission from interaction-powered SNe satisfying $\tau_{pp} \sim 1$ is suppressed at this band.

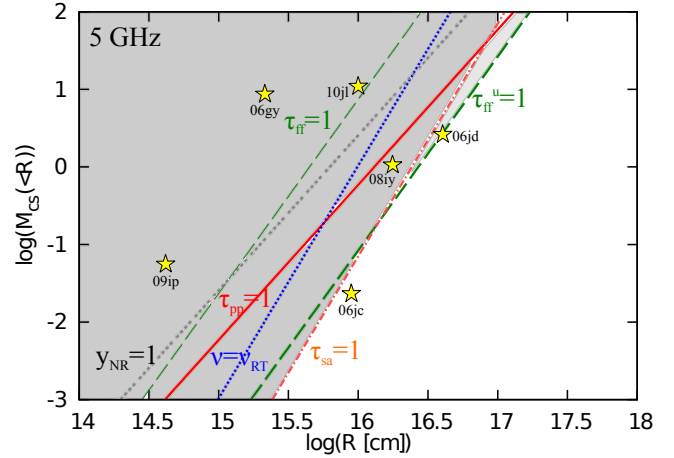


Figure 7. The same as Figure 6, but for the (R, M_{CS}) plane, where M_{CS} has the solar-mass unit.

The line of $\nu = \nu_{\text{RT}}$ is shown in Figures 6-11. Instead, given a frequency, we can obtain the upper limit on D_* as

$$D_{*, -1} \lesssim 1.3 \times 10^3 \mu_e^2 \epsilon_{B,-2} R_{16}^2 (V_s/5000 \text{ km s}^{-1})^2 \nu_{11}^2. \quad (61)$$

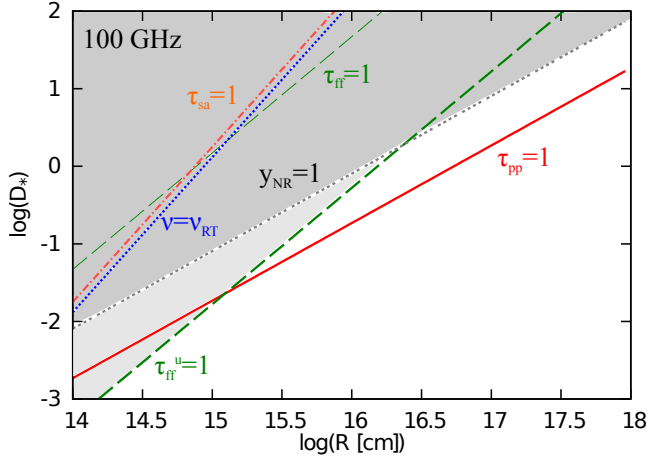


Figure 8. The same as Figure 6, but at $\nu = 100$ GHz. From this figure, one sees that observations at 100 GHz are useful for probing interaction-powered SNe satisfying $\tau_{pp} \sim 1$.

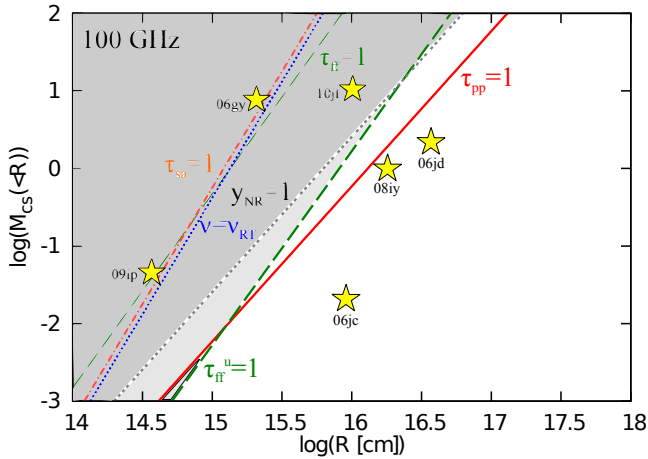


Figure 9. The same as Figure 8, but for the (R, M_{cs}) plane, where M_{cs} has the solar-mass unit.

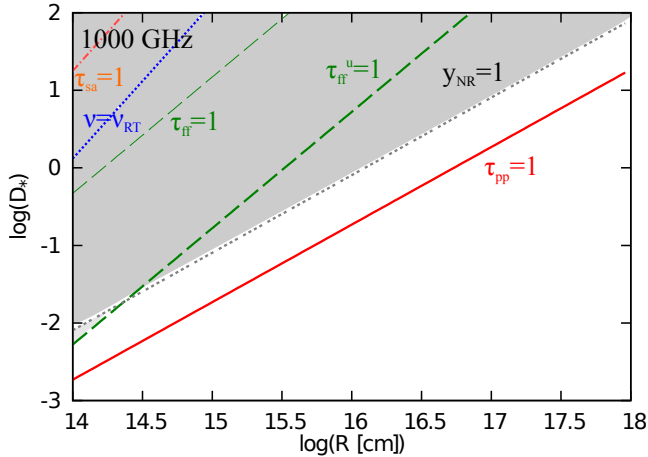


Figure 10. The same as Figure 6, but at $\nu = 1000$ GHz.

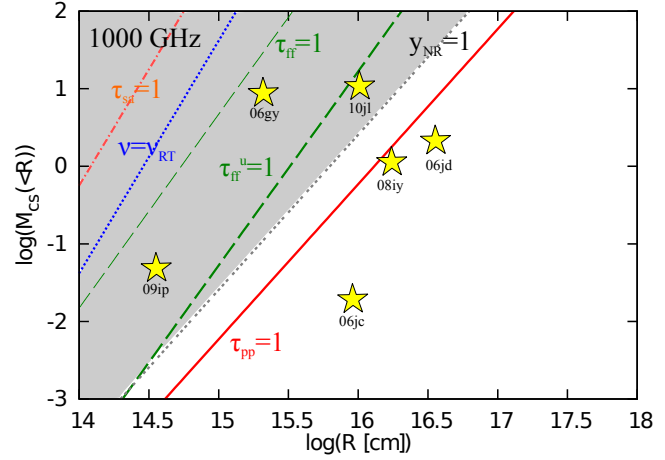


Figure 11. The same as Figure 10, but for the (R, M_{cs}) plane, where M_{cs} has the solar-mass unit.

4.2 Synchrotron self-absorption

The SSA opacity is estimated to be (see Appendix B)

$$\tau_{sa}(\nu) \approx \tau_{sa0} \begin{cases} (\nu/\nu_n)^{-\frac{5}{3}}, & (\nu < \nu_n) \\ (\nu/\nu_n)^{-\frac{p+4}{2}}, & (\nu_n \leq \nu) \end{cases} \quad (62)$$

where p is the spectral index of electrons (that is generally different from q for injected particles), $\nu_n \approx \gamma_n^2 eB/(m_e c)$, and

$$\tau_{sa0} = \xi_p \frac{en_{CRe}}{B\gamma_n^5} R. \quad (63)$$

Here, when the Coulomb cooling is irrelevant, $\gamma_n = \min[\gamma_i, \gamma_c]$ and ξ_p is evaluated as a function of p , which is order of $\sim 5 - 10$ (see Appendix B). When only synchrotron and IC (in the Thomson regime) losses are relevant, we have $p = 2$ at $\gamma_c < \gamma_e < \gamma_i$ in the fast cooling case or $p = q$ when $\gamma_i < \gamma_e < \gamma_c$ (i.e., the slow cooling case). Here, n_{CRe} is related to the number of electrons swept by the shock as

$$N_{CRe} = 4\pi R^3 n_{CRe} \equiv \tilde{f} \frac{\mathcal{E}}{m_p c^2}, \quad (64)$$

where \tilde{f} is the number fraction of electrons defined against $\mathcal{E}/(m_p c^2)$. Note that, for primary electron acceleration, the different parameter f_e satisfies

$$N_{CRe} = f_e \frac{4\pi DR}{m_H}. \quad (65)$$

Assuming a power-law injection spectrum, we have

$$\tilde{f}_e = \frac{\epsilon_e}{\gamma_l \ln(\gamma_e^M/\gamma_l)} \frac{m_p}{m_e}, \quad (66)$$

for $q = 2$ and

$$\tilde{f}_e = \frac{\epsilon_e(q-2)}{\gamma_l(q-1)} \frac{m_p}{m_e}, \quad (67)$$

for $q > 2$, and we typically expect $\tilde{f}_e \sim 3 \times 10^{-3} \epsilon_{e,-3}$. For secondary electrons, we have

$$\tilde{f}_{\pm} = \frac{\min[1, f_{pp}] \epsilon_p m_p}{6\gamma_h \ln(\gamma_p^M)} \frac{m_p}{m_e}, \quad (68)$$

for $q = 2$ and

$$\tilde{f}_{\pm} = \frac{\min[1, f_{pp}] \epsilon_p (q-2) m_p}{6\gamma_h (q-1) m_e}, \quad (69)$$

for $q > 2$. The proton spectrum is assumed to be a power law above $m_p c^2$, where we typically obtain $\tilde{f}_{\pm} \sim 3 \times 10^{-3} \epsilon_{p,-1} \min[10, f_{pp,-1}]$. Introducing \tilde{f} allows us to discuss primary and secondary electrons in parallel.

Setting $\tau_{sa} = 1$, the SSA frequency is estimated to be

$$\begin{aligned} \nu_{sa} &\sim 9.0 \times 10^9 \text{ Hz } \tilde{f}_{-2.5}^{1/3} \epsilon_{B,-2}^{1/3} D_{*, -1}^{2/3} \\ &\times R_{16}^{-1} (V_s/5000 \text{ km s}^{-1})^{4/3} \gamma_{n,1.5}^{1/3}, \end{aligned} \quad (70)$$

for $p = 2$ (leading to $\xi_p \simeq 8.773$), and

$$\begin{aligned} \nu_{sa} &\sim 1.1 \times 10^{10} \text{ Hz } \tilde{f}_{-2.5}^{2/7} \epsilon_{B,-2}^{5/14} D_{*, -1}^{9/14} \\ &\times R_{16}^{-1} (V_s/5000 \text{ km s}^{-1})^{9/7} \gamma_{n,1.5}^{4/7}, \end{aligned} \quad (71)$$

for $p = 3$ (leading to $\xi_p \simeq 26.31$). Instead, given a frequency, we can obtain the upper limit on D_* as

$$\begin{aligned} D_{*, -1} &\lesssim 37 \tilde{f}_{-2.5}^{-1/2} \epsilon_{B,-2}^{-1/2} R_{16}^{3/2} \\ &\times (V_s/5000 \text{ km s}^{-1})^{-2} \gamma_{n,1.5}^{-1/2} \nu_{11}^{3/2}, \end{aligned} \quad (72)$$

for $p = 2$, and

$$\begin{aligned} D_{*, -1} &\lesssim 32 \tilde{f}_{-2.5}^{-4/9} \epsilon_{B,-2}^{-5/9} R_{16}^{14/9} \\ &\times (V_s/5000 \text{ km s}^{-1})^{-2} \gamma_{n,1.5}^{-8/9} \nu_{11}^{14/9}, \end{aligned} \quad (73)$$

for $p = 3$. Note that we should use $\gamma_n = \gamma_c \propto D^{-1} R$ and $p = 2$ for the fast cooling case. Results for $q = 2$ and $q = 3$ are shown in Figures 6-11. In this work, we assume the case of $\nu_{sa} < \nu_b = \max[\nu_c, \nu_i]$, although SSA heating is relevant when $\nu_{sa} > \nu_b = \max[\nu_c, \nu_i]$ (Murase et al. 2014).

4.3 Free-free absorption

The free-free absorption is important especially when photons propagate in the ionized plasma. For simplicity, here we assume that ions are protons. In the hot downstream, the free-free opacity for photons with $h\nu < kT_e$ is (Rybicki & Lightman 1986)

$$\begin{aligned} \tau_{ff}(\nu) &\approx \sigma \alpha_{ff} R \\ &\simeq 6.4 \times 10^{-5} \bar{g}_{ff} T_{e,8}^{-3/2} \mu_e^{-1} D_{*, -1}^2 R_{16}^{-3} \nu_{11}^{-2}, \end{aligned} \quad (74)$$

where α_{ff} is the free-free absorption coefficient and \bar{g}_{ff} is the Gaunt factor. High temperatures of $T_e \sim 10^8$ K are expected in the immediate downstream, while the temperature is lower at the far downstream due to bremsstrahlung cooling especially if the shock is radiative. The free-free absorption frequency is given by $\tau_{ff} = 1$, and we have

$$\nu_{ff} \simeq 8.0 \times 10^8 \text{ Hz } \bar{g}_{ff}^{1/2} T_{e,8}^{-3/4} \mu_e^{-1/2} D_{*, -1} R_{16}^{-3/2}. \quad (75)$$

Instead, given a frequency, we can obtain the upper limit on D_* as

$$D_{*, -1} \lesssim 130 \bar{g}_{ff}^{1/2} T_{e,8}^{3/4} \mu_e^{1/2} R_{16}^{3/2} \nu_{11}. \quad (76)$$

If the free-free absorption in the emission region is dominant, we expect the suppression factor of $1/\tau_{ff} \propto \nu^2$ at $\nu < \nu_{ff}$.

However, one typically expects that upstream material would be more crucial for absorbing low-frequency emission (but see Chandra et al. 2012a). The upstream temperature is lower than the immediate downstream temperature, so the free-free optical depth can be much larger. Before the shock reaches R_w , assuming ionized material, the free-free optical depth in the upstream is

$$\begin{aligned} \tau_{ff}^u(\nu) &\approx \alpha_{ff} R \\ &\simeq 5.0 \times 10^{-1} \bar{g}_{ff}(T_{e,5}^u)^{-3/2} \mu_e^{-1} D_{*, -1}^2 R_{16}^{-3} \nu_{11}^{-2}, \end{aligned} \quad (77)$$

The free-free absorption frequency is given by $\tau_{ff}^u = 1$, and we have

$$\nu_{ff} \simeq 7.1 \times 10^{10} \text{ Hz } \bar{g}_{ff}^{1/2} (T_{e,5}^u)^{-3/4} \mu_e^{-1/2} D_{*, -1} R_{16}^{-3/2}. \quad (78)$$

Instead, given a frequency, we can obtain the upper limit on D_* as

$$D_{*, -1} \lesssim 1.4 \bar{g}_{ff}^{1/2} (T_{e,5}^u)^{3/4} \mu_e^{1/2} R_{16}^{3/2} \nu_{11}. \quad (79)$$

Note that, if the free-free absorption in the screen region is dominant, we expect the suppression of $\exp(-\tau_{ff}^u)$, which can be in principle distinguished from the other possibilities. As shown in Figures 8 and 9, at ~ 100 GHz, the free-free absorption is typically the most important attenuation process in SNe with dense CSM. Even at ~ 5 GHz, it is the dominant attenuation process for ejecta-CSM interactions at $\gtrsim 10^{16}$ cm. This process is sensitive to the electron temperature, and $T_e^u = 10^5$ K is used in Figures 6-11. The temperature may indeed be high enough, as suggested by successful radio detections of SN 2006jd (Chandra et al. 2012a). In Figure 7, SN 2006jd¹⁰ lies near the lines of $\tau_{ff}^u = 1$ and $\tau_{sa} = 1$. On the other hand, non-detections of radio emission from many other Type II In SNe like SN 2010jl seem consistent with the large absorption that is easily realized with more conservative values of $T_e^u \sim 10^4$ K (Chandra et al. 2012b; Ofek et al. 2014).

At ~ 5 GHz, as shown in Figures 6 and 7, the free-free absorption and SSA processes suppress radio signals, and the parameter space around $\tau_{pp} \sim 1$ is located in the dark shaded area. So it is difficult to see hadronic signatures with synchrotron emission at radio wavelengths. But the situation drastically changes at higher frequencies. At ~ 100 GHz, the free-free absorption is still an obstacle for ejecta-CSM interactions at $\lesssim 10^{16}$ cm, but not for $\gtrsim 10^{16}$ cm. Importantly, as shown in Figures 8 and 9, a large parameter space of $\tau_{pp} \sim 1$ is free of absorption and scattering processes. So observations at high-frequency radio wavelengths including mm/submm and FIR bands are indeed powerful to test the hadronic model and probe cosmic-ray proton acceleration. At higher frequencies such as 1000 GHz, all the absorption processes discussed here are negligible compared to the Comptonization due to thermal electrons. Not all interaction-powered SNe allow us to expect high-frequency radio signals from secondaries. As pointed out by Murase et

¹⁰ While SN 2006jd lies around the light shaded area in Figure 7, the observed radio spectrum may not be consistent with the free-free absorption in the screen zone (Chandra et al. 2012a).

al. (2011), except at sufficiently late phases, optically-bright SLSNe are difficult to detect with synchrotron emission at radio bands. On the other hand, as shown in Figures 9 and 11, some Type IIn SNe such as SN 2006jd and 2008iy seem very promising.

There are some possibilities that we have effectively lower values of τ_{ff}^u . First, the CSM may be anisotropic or clumpy as suggested in several Type IIn SNe like SN 2005ip (Smith et al. 2009) and 2009ip (e.g., Margutti et al. 2014), where the emission more easily escape from partial regions where the CSM density is much lower. Secondly, τ_{ff}^u is smaller when the CSM is little ionized, which may be realized especially in the far upstream. This is different from soft X rays that are more strongly absorbed in the non-ionized CSM. Such more transparent cases correspond to the light shaded area in Figures 6-11.

Note that the free-free optical depth declines after the shock reaches the outer edge of CSM, R_w . After $R \gtrsim R_w$, it becomes

$$\begin{aligned} \tau_{\text{ff}}^u(\nu) &= \int_{R_w} dr \alpha_{\text{ff}} \\ &\simeq 5.0 \times 10^{-2} \left(\frac{10}{2s' - 1} \right) \bar{g}_{\text{ff}}(T_{e,5}^u)^{-3/2} \mu_e^{-1} D_{*, -1}^2 \\ &\times R_{w,16}^{-3} (R_w/R)^{2s'-1} \nu_{11}^{-2}, \end{aligned} \quad (80)$$

where $\rho_{\text{cs}} \propto R^{-s'}$ (at $R > R_w$) is assumed. For example, a possible value of $s' \sim 5 - 6$ is suggested in the late phase of the re-brightening of SN 2009ip (Margutti et al. 2014).

5 SUMMARY

In this work, we provide a broad discussion of multi-messenger diagnoses of interaction-powered SNe including Type IIn SNe and some SLSNe, focusing on non-thermal signals. The shock would be radiation-mediated at very early times, and thus CR acceleration is inefficient. However, as photons escape the system, a collisionless shock can form and CR acceleration becomes possible. While shock heating leads to X rays, CRs are expected to produce broadband non-thermal emission, including gamma rays, X rays, radio waves and neutrinos.

Photon emission in general may be largely thermalized depending the optical depth, which in turn depends on details of the CSM. Neutrinos are the most direct probe in the sense that they do not suffer from attenuation in the source. In addition, by advancing the idea proposed by Murase et al. (2011), we have shown that GeV gamma rays can typically escape after the shock breakout, although TeV gamma rays are attenuated due to the two-photon annihilation process¹¹. Along with neutrinos, GeV gamma rays can provide unique opportunities to probe the formation of collisionless shocks and the onset of CR acceleration. Interestingly,

the physical parameters suggested by observed interaction-powered SNe imply densities similar to those inferred from gamma-ray novae (Abdo et al. 2010), allowing us to expect analogous high-energy emission and to probe the physics of CR acceleration in the dense environment. Detecting signals from one SN requires a nearby event, but stacking analyses are still useful. Gamma rays and neutrinos are especially powerful for optically-bright SLSNe, for which the recipes provided in Appendix A can be used.

For normal luminosity interaction-powered SNe, broadband non-thermal emissions from radio to TeV gamma-ray bands are possible. In particular, high-frequency radio observations in the mm/submm and FIR bands can probe CR proton acceleration and test the hadronic model. We pointed out that secondary electrons produced via pp reactions play an important pole role in the synchrotron emission from some interaction-powered SNe such as SN 2006jd. Comprehensive observations from GHz to 1000 GHz may also be relevant to study acceleration of primary electrons that may not be accelerated by the conventional shock acceleration. Our work demonstrates the importance of multi-messenger approaches in revealing the mechanism of Type IIn SNe and CR acceleration in real time.

The interaction-powered SN scenario has been commonly used to interpret SLSNe, but SLSNe are diverse and other scenarios also possible. For example, some SLSNe such as SN 2007bi may be rather pair-instability SNe originating from progenitors with $M_* \gtrsim 130M_\odot$, where the stellar collapse is caused by the pressure decrease due to electron-positron pair-production (Gal-Yam & Leonard 2009; Gal-Yam et al. 2009). Or luminous SNe including SLSNe Ic (e.g., Chornock et al. 2013) may be driven by newborn pulsars (e.g., Kasen & Bildsten 2010; Metzger et al. 2011; Woosley 2010). Some SLSNe seem difficult to explain using these scenarios (Gal-Yam 2012; Inserra et al. 2013). High-energy emissions including gamma rays and neutrinos have been predicted in both the interaction-powered SN scenario (Murase et al. 2011; Katz et al. 2011) and the pulsar-driven SN scenario (Murase et al. 2009; Kotera et al. 2013). Detecting thermal and non-thermal signals from shocks in the dense CSM and studying time-dependent spectra are crucial in order to discriminate among the scenarios.

The most important point of this work is that secondary electrons and positrons from inelastic pp collisions will radiate detectable synchrotron photons efficiently at high-frequency radio wavelengths including the mm/submm and FIR bands. Although details depend on the mass of CSM, its physical location relative to the progenitor star at the time of explosion, and the velocity of the ejecta, for typical parameters, we expect the synchrotron spectrum to peak at $\sim 3 - 3000$ GHz and with flux of $\sim 0.01 - 0.1$ mJy for 2006jd-like interaction-powered SNe at distances of hundreds of Mpc. In particular, high-frequency radio signals using instruments like the high-frequency channels of the VLA and ALMA can be very powerful to probe physics of collisionless shocks. For this reason, we encourage followup observations especially at the mm/submm band within months-to-years and at the GeV-TeV gamma-ray band within days-to-years.

¹¹ Note that Model A in Murase et al. (2011) considered a different situation before breakout of the forward shock emission.

ACKNOWLEDGMENTS

K. M. thanks John Beacom, Roger Chevalier, Boaz Katz, Brian Lacki, Keiichi Maeda, Jose Prieto, Masaomi Tanaka and Ryo Yamazaki for useful discussions. K. M. is supported by NASA through Hubble Fellowship, Grant No. 51310.01 awarded by the Space Telescope Science Institute, which is operated by the Association of Universities for Research in Astronomy, Inc., for NASA, under Contract No. NAS 5-26555. K. M. also thanks supports by CCAPP since this project was started in the beginning of 2011 when K. M. was a member of CCAPP. The preliminary results of this work was presented in March 2013, Hubble Fellows Symposium.

**APPENDIX A: RECIPES FOR TESTING
BREAKOUT HIGH-ENERGY EMISSION IN
THE INTERACTION-POWERED SN
SCENARIO**

Here, we provide recipes to test the hadronic model for gamma-ray and neutrino emissions from interaction-powered SNe. Basically, we need to know two quantities, the CR energy \mathcal{E}_{CRp} and the pp efficiency f_{pp} . The latter depends on n_{cs} , R and V_s , which can be determined from the breakout emission.

The more sophisticated approach is possible based on self-similar solutions in the engine-driven case (Chevalier 1982a). We here overview the prescription by Chevalier & Irwin (2011). Let us consider the ejecta whose outer density profile is $\rho_{ej} = Ct^{-3}(R/t)^{-7}$ at $V_r > V_t = (2\mathcal{E}_{ej}/M_{ej})^{1/2}$. The shock is initially radiation-mediated and the flows are radiation-dominated since $\tau_T \gg (c/V_s)$. The contact discontinuity is located at $R_{cd} = (0.227C/D)^{1/5}t^{4/5}$, where $C = 4\mathcal{E}_{ej}^2/(3\pi M_{ej})$. The forward shock radius is estimated to be

$$R_f = 1.208R_{cd} \simeq 0.85 \times 10^{15} \text{ cm } \mathcal{E}_{ej,51}^{2/5} (M_{ej}/10^{0.5} M_\odot)^{-1/5} \times D_*^{-1/5} (t/10 \text{ d})^{4/5} \quad (\text{A1})$$

and the forward shock velocity is $V_f = (4/5)R_f/t \simeq 7800 \text{ km s}^{-1} \mathcal{E}_{ej,51}^{2/5} (M_{ej}/10^{0.5} M_\odot)^{-1/5} D_*^{-1/5} (t/10 \text{ d})^{-1/5}$. The energy carried by the interacting shell is estimated to be $\mathcal{E} \approx 4\mathcal{E}_{ej}^2/(3M_{ej}V_0^2)$, where $V_0 \approx R_r/t \simeq 7900 \text{ km s}^{-1} \mathcal{E}_{ej,51}^{2/5} (M_{ej}/10^{0.5} M_\odot)^{-1/5} D_*^{-1/5} (t/10 \text{ d})^{-1/5}$. For $\hat{\gamma} = 4/3$, the radiation energy is $\mathcal{E}_{rad} = 0.32\mathcal{E}$, so we have

$$\mathcal{E}_{rad} \simeq 1.1 \times 10^{50} \text{ erg } \mathcal{E}_{ej,51}^{6/5} (M_{ej}/10^{0.5} M_\odot)^{-3/5} D_*^{2/5} (t/10 \text{ d})^{2/5}. \quad (\text{A2})$$

In the wind case, the photon diffusion timescale is comparable to the breakout time, and we have

$$t_{\text{rise}} \approx \frac{R_{bo}}{V_f} \approx \frac{\sigma_T}{\mu_e m_H c} \frac{D}{c} \simeq 7.7 \text{ d } \mu_e^{-1} D_*, \quad (\text{A3})$$

as long as the breakout happens at $R_{bo} \ll R_w$. The breakout radius can also be estimated from the evolution of the radiation luminosity and temperature if the black-body approximation is valid, or if V_f is known.

As a result, if we can observe \mathcal{E}_{rad} , t_{rise} and V_f (or R_{bo}), we can evaluate D , $\mathcal{E}_{ej}^2/M_{ej}$ and μ_e as (Margutti et al. 2014)

$$D_* \simeq 2.9 \mathcal{E}_{rad,51} (t_{\text{rise}}/10 \text{ d})^2 R_{bo,15}^{-3}, \quad (\text{A4})$$

$$\mathcal{E}_{ej,51}^2 / (M_{ej}/10^{0.5} M_\odot) \simeq 17 \mathcal{E}_{rad,51} (t_{\text{rise}}/10 \text{ d})^{-2} R_{bo,15}^2, \quad (\text{A5})$$

$$\mu_e^{-1} \simeq 0.45 \mathcal{E}_{rad,51}^{-1} (t_{\text{rise}}/10 \text{ d})^{-1} R_{bo,15}^3. \quad (\text{A6})$$

One should keep in mind that the engine-driven self-similar solution is valid as long as $V_r > V_t$.

Then, we can estimate n_{cs} , allowing us to calculate f_{pp} and resulting neutrino and gamma-ray spectra. There are two important free parameters, the CR spectral index (q_p) and CR energy (\mathcal{E}_{CRp}). For $q_p = 2$, the CR proton spectrum is given by

$$E_p^2 \frac{dN_p}{dE_p} \equiv \frac{\mathcal{E}_{CRp}}{\mathcal{R}_p} = \frac{\mathcal{E}_{CRp}}{\ln(E_p^M/E_p^m)} \quad (\text{A7})$$

and $\mathcal{R}_p \sim 15$ for our typical parameters. For $q_p > 2$, we have

$$E_p^2 \frac{dN_p}{dE_p} \equiv \frac{\mathcal{E}_{CRp}}{\mathcal{R}_p(E_p)} = (q_p - 2) \left(\frac{E_p}{E_p^m} \right)^{2-q_p} \mathcal{E}_{CRp}. \quad (\text{A8})$$

Here, \mathcal{R}_p is the conversion factor from the total energy to the differential energy spectrum and $E_p^m \sim m_p c^2$ is the minimum proton energy. These equations can be rewritten as

$$E_p^2 \frac{dN_p}{dE_p} \equiv \mathcal{R}_{p0}^{-1} \left(\frac{E_p}{E_p^m} \right)^{2-q_p} \mathcal{E}_{CRp}, \quad (\text{A9})$$

where $\mathcal{R}_{p0} \equiv \mathcal{R}_p(E_p^m)$. The CR energy is parametrized as

$$\mathcal{E}_{CRp} = \epsilon_p \mathcal{E} = (\epsilon_p/\epsilon_\gamma) \mathcal{E}_{rad}, \quad (\text{A10})$$

where $\epsilon_p/\epsilon_\gamma$ is the CR loading parameter that is commonly introduced in the literature of hadronic emissions from gamma-ray bursts (Murase & Nagataki 2006). Since both ϵ_p and ϵ_γ are order of 0.1, we expect $\epsilon_p/\epsilon_\gamma \sim 1$ and we can make predictions for breakout high-energy emissions, based on observational quantities. Such an application was done in Margutti et al. (2013). Note that high-energy emissions continue after the breakout. Given sufficient time-dependent data, later contributions can easily be taken into account by more detailed modeling. For example, one can directly use self-similar solutions for $\hat{\gamma} = 4/3$ or $\hat{\gamma} = 5/3$ at $\tau_T \lesssim c/V_s$ (Chevalier & Irwin 2011; Ofek et al. 2014). Most naively, instead, the overall contribution can be incorporated in the CR loading parameter.

**APPENDIX B: FORMULAS OF
SYNCHROTRON SELF-ABSORPTION**

Here we provide formulas to calculate SSA. For a power-law electron distribution, the SSA coefficient is (Rybicki & Lightman 1986)

$$\alpha_{sa}(\nu) = \mathcal{N}_0 \frac{\sqrt{3}e^3}{8\pi m_e} \left(\frac{3e}{2\pi m_e^3 c^5} \right)^{p/2} (B \sin \theta_B)^{(p+2)/2} \times \Gamma(p/4 + 11/6) \Gamma(p/4 + 1/6) \nu^{-(p+4)/2}, \quad (\text{B1})$$

where θ_B is the angle between the electron velocity and magnetic field. The normalization is determined by

$$\int_{\gamma_n} d\gamma_e \mathcal{N}_0 \gamma_e^{-p} = n_{\text{CRE}}. \quad (\text{B2})$$

Assuming $\gamma_b = \max[\gamma_i, \gamma_c] \gg \gamma_n = \min[\gamma_i, \gamma_c]$, we have $\mathcal{N}_0 \approx \xi_p n_{\text{CRE}} \gamma_n^{p-1}$, where $\xi_p = p - 1$ for $p > 1$ and $\xi_p = \ln(\gamma_b/\gamma_n)$ for $p = 1$. When only the synchrotron emission is relevant, we have $p = 2$ at $\gamma_c < \gamma_e < \gamma_i$ in the fast cooling case or $p = q$ at $\gamma_i < \gamma_e < \gamma_c$ in the slow cooling case. Averaged over θ_B , the SSA coefficient is written as

$$\alpha_{\text{sa}}(\nu) = \xi_p \frac{e n_{\text{CRE}}}{B \gamma_n^5} (\nu/\nu_n)^{-(p+4)/2}, \quad (\text{B3})$$

where

$$\begin{aligned} \xi_p &= \tilde{\xi}_p \frac{\pi^{3/2} 3^{(p+1)/2}}{4} \Gamma(p/4 + 11/6) \Gamma(p/4 + 1/6) \\ &\times \frac{\Gamma(p/4 + 3/2)}{\Gamma(p/4 + 2)}. \end{aligned} \quad (\text{B4})$$

For example, we obtain $\xi_2 \simeq 8.773$ for $p = 2$ and $\xi_3 \simeq 26.31$ for $p = 3$, respectively.

Note that the spectrum in the optically-thick limit is obtained from $F_\nu = \pi(j_\nu^{\text{syn}}/\alpha_{\text{sa}})(R^2/d^2) \propto \nu^{5/2}$, where j_ν^{syn} is the synchrotron emissivity (Rybicki & Lightman 1986). The coefficient agrees with Katz (2012). One should keep in mind that the $F_\nu \propto \nu^{5/2}$ is obtained only if $\nu_{\text{sa}} > \nu_n$, whereas we expect $F_\nu \propto \nu^2$ if $\nu_{\text{sa}} < \nu_n$.

REFERENCES

Abdo, A. A. et al., 2010, *Science*, 329, 817
 Ahrens, J. et al., 2004, *Astropart. Phys.*, 20, 507
 Abeysekara, A. U. et al., 2013, *Astropart. Phys.*, 50, 26
 Balberg, S., Loeb, A., 2012, *MNRAS*, 414, 1715
 Bell A. R., 2004, *MNRAS*, 353, 550
 Bell, A. R., 2013, *Astropart. Phys.*, 43, 56
 Bykov, A. M., Brandenburg, A., Malkov, M. A., Osipov, S. M., 2013, *Space Sci. Rev.*, 178, 201
 Budnik, R., Katz, B., MacFadyen, A., Waxman, E., 2008, *ApJ*, 673, 928
 Caprioli, D., Blasi, P., Amato, E., 2009, *MNRAS*, 396, 2065
 The CTA Consortium, 2011, *Experimental Astronomy*, 32, 193
 Chandra, P., Chevalier, R. A., Chugai, N., Fransson, C., Irwin, C. M., Soderberg, A. M., Chakraborti, S., Immler, S., 2012a, *ApJ*, 755, 110
 Chandra, P., Chevalier, R. A., Irwin, C. M., Chugai, N., Fransson, C., Soderberg, A. M., 2012b, *ApJ*, 750, L2
 Chevalier, R. A., 1982a, *ApJ*, 258, 790
 Chevalier, R. A., 1982b, *ApJ*, 259, 302
 Chevalier, R. A., 1984, *ApJ*, 285, L63
 Chevalier, R. A., 1998, *ApJ*, 499, 810
 Chevalier R. A., Fransson C., 2003, in Weiler K., ed., *Lecture Notes in Physics Vol. 598, Supernovae and Gamma-Ray Bursters*. Springer-Verlag, Berlin, p. 171
 Chevalier, R. A., Irwin, C. M., 2011, *ApJ*, 729, L6
 Chevalier, R. A., Irwin, C. M., 2012, *ApJ*, 747, L17

Chodorowski, M. J., Zdziarski, A. A., Sikora, M., 1992, *ApJ*, 400, 181
 Chornock, R. et al., 2013, *ApJ*, 767, 162
 Chugai, N. N., Danziger, I. J., 1994, *MNRAS*, 268, 173
 Dermer, C. D., 1986, *ApJ*, 307, 47
 Drury, L. O., 1983, *Rep. Prog. Phys.*, 46, 973
 Drury L. O., 2011, *MNRAS*, 415, 1807
 Falk, S. W. and Arnett, W. D., 1973, *ApJ*, 180, L65
 Fransson, C., Lundqvist, P., Chevalier, R. A., 1996, *ApJ*, 461, 993
 Fransson, C. et al., 2013, arXiv:1312.6617
 Funk, S., Hinton, J. A., for the CTA Consortium, 2013, *Astropart. Phys.*, 43, 348
 Gal-Yam, A., 2012, *Science*, 337, 927
 Gal-Yam, A., Leonard D. C., 2009, *Nature (London)*, 458, 865
 Gal-Yam, A. et al., 2009, *Nature (London)*, 462, 624
 Immler, S. et al., 2008, *ApJ*, 674, L85
 Inoue, T., Yamazaki, R., Inutsuka, S., 2009, *ApJ*, 695, 825
 Inoue, T., Yamazaki, R., Inutsuka, S., Fukui, Y., 2012, *ApJ*, 744, 71
 Inserra, C. et al., 2013, *ApJ*, 770, 128
 Kasen D., Bildsten L., 2010, *ApJ*, 717, 245
 Kashiyama, K., Murase, K., Horiuchi, S., Gao, S., Mészáros, P., 2013, *ApJ*, 769, L6
 Katz, B., 2012, *MNRAS*, 420, L6
 Katz, B., Budnik, R., Waxman, E., 2010, *ApJ*, 716, 781
 Katz, B., Sapir, N., Waxman, E., 2011, arXiv:1106.1898
 Katz, B., Waxman, E., 2008, *JCAP*, 01, 018
 Kotera, K., Phinney, E. S., Olinto, A. V., 2013, *MNRAS*, 432, 3228
 Kulsrud, R. M., Cesarsky, C. J., 1971, *AL*, 8, 189
 Maeda, K., 2012, *ApJ* 758, 81
 Mauerhan, J. C. et al., 2013, *MNRAS*, 430, 1801
 Metzger, B. D., Giannios, D., Thompson, T. A., Bucciantini, N., Quataert, E., 2011, *MNRAS*, 413, 2031
 Miller, A. A. et al., 2009, *ApJ*, 690, 1303
 Miller, A. A. et al., 2010, *MNRAS*, 404, 305
 Margutti, R. et al., 2014, *ApJ*, 780, 21
 Moriya, T. J., Blinnikov, S. I., Tominaga, N., Yoshida, N., Tanaka, M., Maeda, K., Nomoto, K., 2013a, *MNRAS*, 428, 1020
 Moriya, T. J., Maeda, K., Taddia, F., Sollerman, J., Blinnikov, S. I., Sorokina, E. I., 2013b, *MNRAS*, 435, 1520
 Murase, K., Mészáros, P., Zhang, B., 2009, *Phys. Rev. D*, 79, 103001
 Murase, K., Nagataki, S., 2006, *Phys. Rev. D*, 73, 063002
 Murase, K., Thompson, T. A., Lacki, B. C., Beacom, J. F., 2011, *Phys. Rev. D*, 84, 043003
 Murase, K. et al., 2014, in preparation
 Ofek, E. O., Lin, L., Kouveliotou, C., Younes, G., Göögüs, E., Kasliwal, M. M., Cao, Y. T., 2013a, *ApJ*, 768, 47
 Ofek, E. O. et al., 2007, *ApJ*, 659, L13
 Ofek, E. O. et al., 2013b, *ApJ*, 763, 42
 Ofek, E. O. et al., 2010, *ApJ*, 724, 1396
 Ofek, E. O. et al., 2013c, *Nature (London)*, 494, 65
 Ofek, E. O. et al., 2014, *ApJ*, 781, 42
 Ohira, Y., Murase, K., Yamazaki, R., 2010, *A&A*, 513, A17

- Pan, T., Patnaude, D., Loeb, A., 2013, MNRAS, 433, 838
Pastorello, A. et al., 2013, ApJ, 767, 1
Prieto, J. L., Brimacombe, J., Drake, A. J., Howerton, S., 2013, ApJ, 763, L27
Quimby, R. M. et al., 2011, Nature, 474, 487
Quimby, R. M., Yuan, F., Akerlof, C., Wheeler, J. C., 2013, MNRAS, 431, 912
Rest, A. et al., 2011, ApJ, 729, 88
Rybicki G. B., Lightman A. P., 1986, Radiative Processes in Astrophysics. Wiley, New York
Sari, E., & Esin, A. A., 2001, ApJ, 548, 787
Schlickeiser, R., 2002, Cosmic Ray Astrophysics, (New York: Springer)
Smith, N., 2013, MNRAS, 429, 2366
Smith, N., Chornock, R., Silverman, J. M., Filippenko, A. V., Foley, R. J., 2010, ApJ, 709, 856
Smith, N., Foley, R. J., Filippenko, A. V., 2008, ApJ, 680, 568
Smith, N. et al., 2007, ApJ, 666, 1116
Smith, N., McCray, R., 2007, ApJ, 671, L17
Smith, N. et al., 2009, ApJ, 695, 1334
Sveshnikova, L. G., 2003, A&A, 409, 799
Svirski, G., Nakar, E., Sari, R., 2012, ApJ, 759, 108
Truelove, J. K., McKee, C. F., 1999, ApJS, 120, 299
van Marle, A. J., Smith, N., Owocki, S. P., van Veelen, B., 2010, MNRAS, 407, 2305
Waxman, E., Loeb, A., 2001, Phys. Rev. Lett., 87, 071101
Weaver, T. A., 1976, ApJS, 32, 233
Woosley S. E., 2010, ApJ, 719, L204

This paper has been typeset from a \TeX / \LaTeX file prepared by the author.